CZECH TECHNICAL UNIVERSITY IN PRAGUE

Faculty of Nuclear Sciences and Physical Engineering

Department of Physics

Research project

Study of jet production in Au+Au collisions in the STAR experiment

Bc. Martin Kocmánek

RNDr. Jana Bielčíková Ph.D.

Prague, 2016

Prohlášení:

Prohlašuji, že jsem svůj výzkumný úkol vypracoval samostatně a použil jsem pouze podklady (literaturu, software, atd.) uvedené v přiloženém seznamu.

Nemám závažný důvod proti užití tohoto školního díla ve smyslu 60 Zákona .121/2000 Sb., o právu autorském, o právech souvisejících s právem autorským a o změně některých zákonů (autorský zákon).

V Praze dne

Title:
Study of jet production in Au+Au collisions in the STAR experiment

Author: Martin Kocmánek

Specialization: Experimental nuclear physics

Sort of project: Research project

Supervisor: RNDr. Jana Bielčíková, Ph.D.

Consultant: Ing. Jan Rusňák

Abstract: Ultra-relativistic heavy-ion collisions enable us to create quark-gluon plasma, extremely hot and dense nuclear matter. During hard scattering partons of incoming nuclei undergo fragmentation and hadronisation which results in jets, collimated sprays of hadrons. Due to interaction of hard partons with QGP, the energy of partons is reduced in comparison with p+p collisions, what is referred to as a jet quenching. Measurement of various modifications of jets traversing the medium provides important information about properties of nuclear matter. This research project presents brief introduction to jet physics, recent results of jet analysis at STAR and describes the begining of the analysis of fully reconstructed jets produced in Au+Au collisions at $\sqrt{s_{NN}}$= 200 GeV using data recorded during the 2011 RHIC run. The study of data quality assurance, response of the BEMC and its time stability was performed first. It is followed by application of the anti-k_T jet algorithm as a function of centrality as well as a function of the resolution parameter R to reconstruct uncorrected jet spectra. Then the median of the background energy density was subtracted from jet spectra. Finally, reconstructed full jet spectra were compared with charged jet spectra with p_T cuts on leading hadron of the jet.

Key words: quark-gluon plasma, nucleus-nucleus collisions, jet, jet algorithm, full jet reconstruction, STAR

Názov práce:
Studium produkce jetů v Au+Au zrážkách v experimentu STAR

Autor: Martin Kocmánek

Abstrakt: Ultra-relativistické zrážky ťažkých iónov umožňujú vytvoriť kvark-gluónovú plazmu, extrémne horúcu a hustú jadrovú hmotu. Počas tvrdého rozptylu zrážajúcich sa partónov v jadrách dochádza k ich fragmentácii a hadronizácii, čo vedie k tvorbe jetov, kolimovaných spŕšok hadrónov. Z dôvodu interakcie tvrdých partónov s kvark-gluónovou plazmou, energia partónov môže byť v porovnaní s p+p zrážkami redukovaná, čo je pripisované tzv. zhášaniu jetov. Meranie rôznych modifikácii jetov prechádzajúcich médiom poskytuje dôležité informácie o jadrovej hmote. Tento výskumný projekt obsahuje stručný úvod do fyziky jetov, výsledky analýzy jetov na experimente STAR a opisuje začiatok analýzy plne rekonštruovaných jetov produkovaných v Au+Au zrážkach pri energii $\sqrt{s_{NN}}$= 200 GeV zaznamenaných v roku 2011 na urýchľovači RHIC. Na začiatku bola prevedená štúdia kvality dát z elektromagnetického kalorimetru BEMC, a taktiež jeho odozvy a časovej stability. Následne aplikáciou anti-k_T algoritmu sa rekonštruovali nekorigované plné jetové spektrá ako funkcia centrality zrážky, ako aj rozlišovacieho parametru R. Potom nasledovalo odčítanie mediánu energie hustoty pozadia od jetových spektier. Na konci boli plné jetové spektrá porovnané s nabitými, na ktoré boli aplikované selekčné kritériá na hybnosť vedúceho hadrónu v jete.

Kľúčové slová: kvark-gluonová plazma, jadro-jadrové zrážky, jet, jetový algoritmus, plná jetová rekonštrukcia, STAR

Acknowledgement

I am very grateful to my supervisor RNDr. Jana Bielčíková, Ph.D. for her willingness, patience, support, professional guidance, advices, language corrections and help with this research project. Also I would like to thank to Jan Rusňák for his advices, suggestions and introducing me into jet analysis. And finally, I am grateful to all who supported me, especially my family and friends.

Contents

List of Figures

Chapter 1

Physics of high energy nucleus collisions

1.1 Quark-gluon plasma

In modern nuclear particle physics, many experiments focus on the research of nuclear matter, called quark-gluon plasma (QGP). The quark-gluon plasma is a new state of hot and dense nuclear matter consisting of free partons - quarks and gluons. It is theoretically predicted from the Quantum Chromodynamics (QCD). Asymptotic freedom is a feature of QCD that causes bonds between quarks and gluons to become asymptotically weaker as energy increases and distance decreases. Therefore QGP exists only at extreme high temperature T and baryonic density μ_B in the order of 10^{12} K and 10^{12} kg.cm^{-1} [1], when quarks and gluons are deconfined. Considering these conditions, QGP can be found in three places: in the first microseconds after the Big Bang, in the center of compact stars and finally in ultra-relativistic heavy-ion collisions.

Experiments at the Relativistic Heavy-Ion Collider (RHIC) at BNL and at the Large Hadron Collider (LHC) at CERN are dedicated to achieve such extreme conditions by collisions of accelerated heavy-ions to ultra-relativistic velocities. The relativistic heavy-ion collision is a dynamic process with a typical time scale and size of the order of 10 fm and 10 fm/c. QGP is supposed to be formed in the initial stage of the collision. When the Lorentz contracted nuclei collide, they pass through each other and create a fireball of hot and dense nuclear matter. Immediately after the collision, the fireball starts to expand and new particles are produced which are eventually measured by detectors.

In Figure 1.1 we can see the phase diagram of nuclear matter that is one of the main subjects of current research. The horizontal axis represents baryon chemical potential μ_B and the vertical axis is temperature T. When T and μ_B is low the matter is in a state of hadron gas. By increasing T or μ_B hadron gas transforms to QGP, where the white curve symbolizes the first order transition. This curve ends at a specific point, referred to as a critical point. From this point the crossover region starts, where the phase transition of the second order occurs. The search for the critical point is currently carried out in a dedicated Beam Energy Scan (BES) program at RHIC.

1.2 Geometry of nuclear collision

One of the most important parameters for description of a collision of two nuclei is an impact parameter b. It represents the minimal distance between centers of interacting nuclei in the transverse plane. It has a value from 0 to $R_1 + R_2$ [2], where R_1 and R_2 are radii of the colliding nuclei. Centrality is a quantity related to the impact parameter. According to the value of the impact parameter, collisions can be categorized to distant ($b > 2R$, where R is a radius of nucleus), peripheral ($b < 2R$) and central ($b \approx 0$),

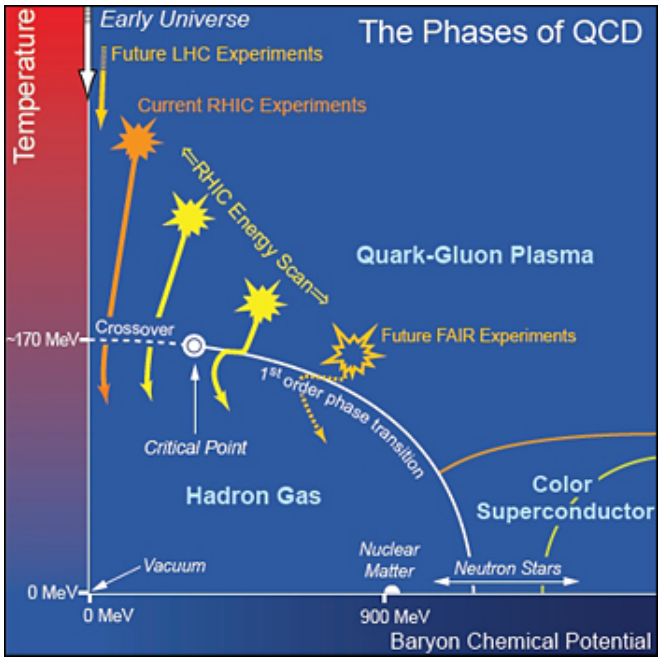

Figure 1.1: A schematic QCD phase diagram of nuclear matter [3].

which are illustrated by Figure 1.2. As the impact parameter decreases, colliding nuclei overlap more and consequently more nucleon-nucleon collisions happen. If a nucleon is involved in a collision with another one, it is referred to as a participant. Nucleons, which do not participate in the collision are referred to as spectators and they continue in the longitudinal direction after the collision. Experimentally, centrality cannot be measured directly, but it is determined from the Glauber model (see next subsection) and multiplicity. Multiplicity represents a total number of produced particles and it is closely related to the centrality. In the case of the central nucleus-nucleus collision with low impact parameter, more nucleons interact among themselves and more particles are produced, which means that multiplicity is higher. Moreover multiplicity is proportional to the energy released in the collision, if the energy of collision is higher then also multiplicity increases. The alternative definition of centrality and its relation to other variables e.g. multiplicity of particles is illustrated in Figure 1.3. Centrality is connected with centrality classes that are defined as percentile of the total geometric cross section in the event according to the impact parameter. Basic centrality classes, which are also depicted in Figure 1.3 are: 0-5% (the most central), 5-10% (central), 10-20% (semi-central), 20-30%(semi-peripheral), 30-50% (peripheral).

1.2.1 Glauber model

Geometry of a heavy-ion collision or the impact parameter, cannot be measured directly. Therefore the impact parameter is determined indirectly from the particle multiplicity, transverse energy or the number of spectator nucleons (measured by "zero-degree calorimeter" ZDC) [4]. The number of participant nucleons N_{part} in the collision can be evaluated by the Glauber model [1]. The Glauber model is used for description of a high-energy heavy-ion collision and calculation of basic geometric variables of the collision such as the number of participant nucleons N_{part} and binary nucleon-nucleon collisions N_{coll} [6]. The Glauber model has two assumptions. The first is that nucleons travel in straight lines without any deflection after the collision. According to this, the Glauber model is a good approximation at very high energies. Secondly, inelastic cross section σ^{in}_{NN} of the nucleon-nucleon collision is the same as in the vacuum. It means that secondary particle production and excitation of nucleons are not taken into

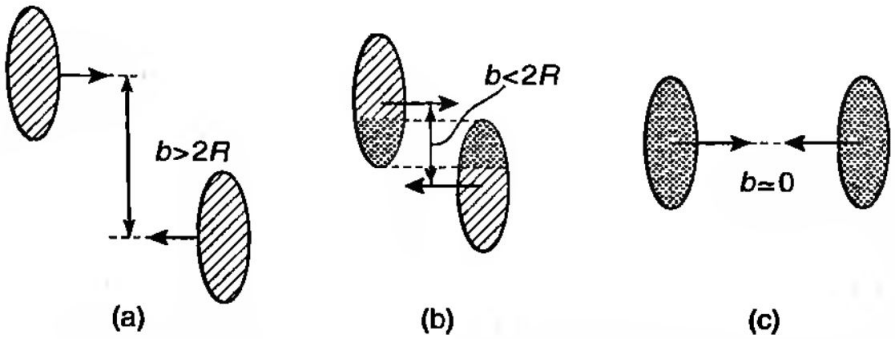

Figure 1.2: Geometry of a nuclear collision according to the value of the impact parameter: (a) - distant collision, (b) - peripheral collision and (c) - central collision. [1]

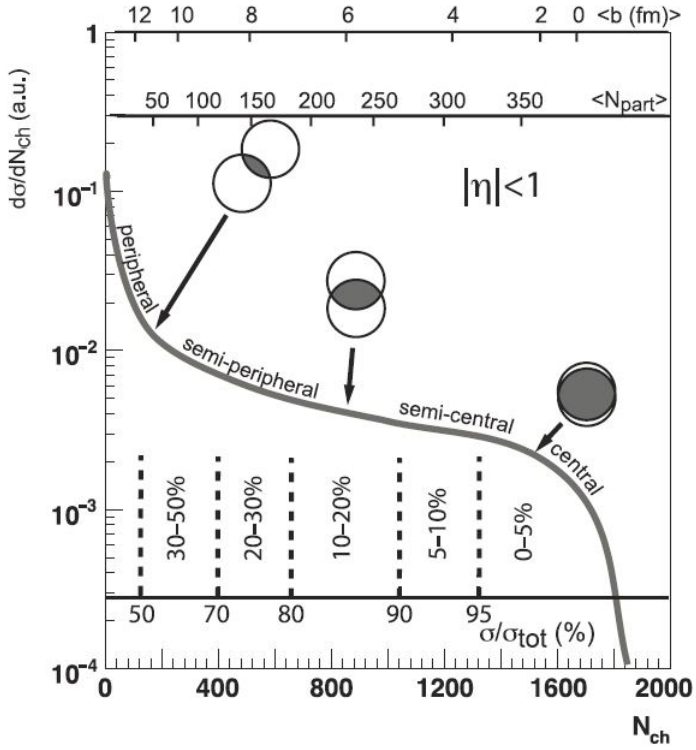

Figure 1.3: Dependence of cross section on number of produced charged particles N_{ch}. The graph also depicts the centrality definition from the final-state particle multiplicity and its correlation with the the impact parameter b, the number of participating nucleons N_{part} in the collision, centrality classes and the ratio of cross section σ in the most central collision to total cross section σ_{tot} of produced particles [5].

account. A collision is treated as multiple nucleon-nucleon interactions. The geometry of variables used in the Glauber model is shown in Figure 1.4. N_{part} and N_{coll} is computed by the Glauber model as follows [1]:

$$N_{part}(b) = \int d^2s\ T_A(s)\left(1 - e^{-\sigma^{in}_{NN}T_B(s)}\right) + \int d^2s\ T_B(s-b)\left(1 - e^{-\sigma^{in}_{NN}T_A(s)}\right) \tag{1.1}$$

$$N_{coll}(b) = \int d^2s\ \sigma^{in}_{NN}T_A(s)T_B(s-b) \tag{1.2}$$

where T_A is the thickness function defined as $T_A(s) = \int dz\rho_A(z,s)$, z is an axis, b is the impact parameter, s is a distance in Figure 1.4, σ^{in}_{NN} inelastic cross section and ρ is the nuclear mass number density ussually given by Wood-Saxon parametrization and normalized to the mass number A. The average N_{part} for a p+p collision is 2, for a p+A collision $N_{part} = N_{coll}+1$ and for an A+A collision N_{part} is calculated by equation 1.1.

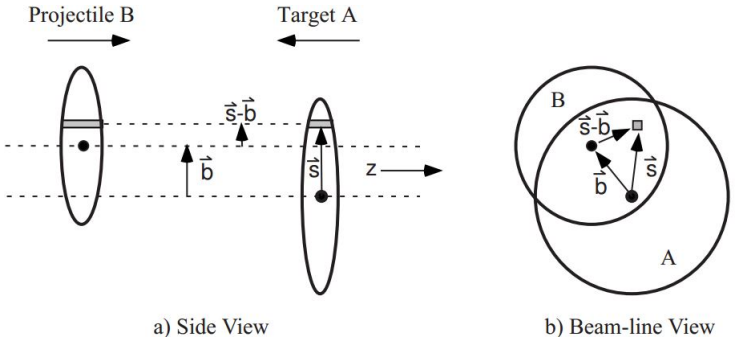

Figure 1.4: A schematic representation of the Glauber model geometry with longitudinal (a) and transverse (b) views [6].

1.3 Space-time evolution of nuclear collision

Medium that is created in an ultra-relativistic heavy-ion collision from the beginning to the time of particle detection undergoes several different phases. The space-time evolution of the initial to final stage is depicted in Figure 1.5.

Immediately after the collision (in the order of femtoseconds) the region of a fireball goes through the following phases: pre-equilibrium, thermalization, hydrodynamical evolution, freeze-out and post-equilibrium [1] Processes in these phases are not completely understood yet and they are the main interest in current research to describe and adequately explain them in theoretical way. The evolution of a nuclear collision is described with the increasing time τ as follows

- $0 < \tau < \tau_0$
  The time 0 expresses the beginning of a collision. Two colliding nuclei traverse each other, they release a large amount of energy and the hot and dense medium of nuclear matter called fireball is immediately formed. The stage of pre-equilibrium is achieved, when the partons are created. This system tends to the state of thermal equilibrium, which cause its fast expansion and the temperature and pressure are decreasing. At the time τ_0 the system might eventually reach thermal equilibrium and the duration of this process is estimated to be about $\tau = 1$ fm/c.

- $\tau_0 < \tau < \tau_f$
  If thermalization is fast enough, then hot and dense nuclear matter, eventually QGP is formed and it reaches a state of local equilibrium. By the stage of thermal equilibrium, the medium behaves as an ideal liquid and the theory of relativistic hydrodynamics can be used for describing this stage and its subsequent progress. After some time of progress of the medium the process of hadronization begins and the medium starts to convert to the hadron gas.

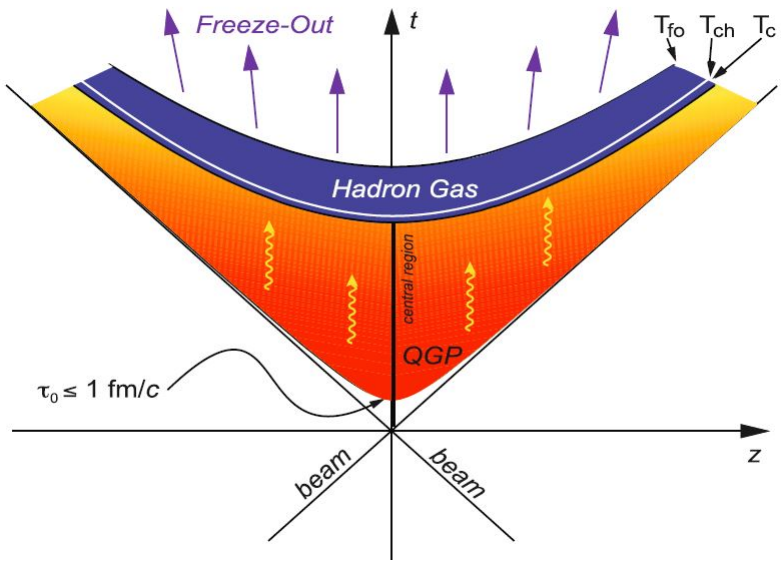

Figure 1.5: Space time evolution of a nuclear collision [3].

- $\tau = \tau_f$
  Free quarks and gluons start to confine to hadrons. It happens at the time of τ_f, when the temperature of QGP falls to the critical value $T_f = 170$ MeV [4]. This effect is also called freeze-out and phase transition between QGP and hadronic matter occurs. But there are two kinds of freeze-out: the chemical, which comes first and has higher temperature than later thermal freeze-out which is also called kinetical freeze-out. During chemical freeze-out particles undergo mutual elastic collisions until the thermal freeze-out comes. In this phase, new particles are not produced anymore and their number stabilize at certain equilibrium with a constant baryochemic potential and temperature. Finally, when the thermal freeze-out takes place, particles fly away from the region of the collision, because the mean free path is almost identical to the size of the system.

- $\tau_f < \tau$
  After time τ_f decoupling starts, particles recede each other and leave region of the collision.

All individual stages of the relativistic heavy-ion collision are schematically depicted in Figure 1.6.

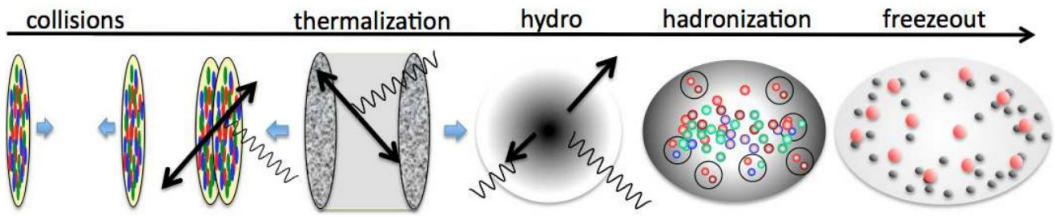

Figure 1.6: Evolution of a heavy-ion collision [7].

1.4 Probes of QGP

In a high energy heavy-ion collision QGP might be created and the probability of its formation depends proportionally on centrality and the center of mass energy of colliding ions. For studying of the presence of QGP and its properties it is necessary to have sensitive probes. The state of a quark gluon plasma created during the collision lasts for a very short time - in the order of tens of fm/c and for this reason its direct detection is very difficult, because only hadrons and leptons in the final state are observable. Thus it is required to find out probes and methods for studying QGP indirectly. Particles that arise from the collision carry important information about properties of QGP and they represent indirect indication of deconfined phase of matter. The most important probes of QGP are elliptic flow, suppression of particles with high p_T, jet quenching, direct photons, dileptons, strangeness enhancement or quarkonium suppression.

1.5 Nuclear Modification Factor

A nuclear modification factor is a convenient tool for probing of QGP quantitatively. The nuclear modification factor expressed by formula 1.3 compares a p_T differential yield of high p_T hadrons or jets in a heavy-ion collision to the differential production cross section in a p+p collision at the same CMS energy $\sqrt{s_{NN}}$.

$$R_{AA}(b, y, p_T) = \frac{1}{\langle T_{AA}(b) \rangle} \frac{\mathrm{d}^2 N_{AA}/\mathrm{d}y\mathrm{d}p_T}{\mathrm{d}^2 N_{pp}/\mathrm{d}y\mathrm{d}p_T} \tag{1.3}$$

T_{AA} is a nuclear overlap function that accounts for the increased parton flux in A+A collisions compared to p+p collisions and it is related to the number of binary nucleon-nucleon collision N_{coll} that are calculated by the Glauber model [8].

If the nuclear modification factor is equal to 1, then there is a minimal difference in yields between p+p and A+A. We do not observe influence of medium on particle production. In the case when $R_{AA} < 1$ it is referred to as a suppression when the number of particles or energy of particles produced in A+A collision is smaler than in p+p and there is expectation of QGP existence. When $R_{AA} > 1$ it denotes enhancement in particle production, known as Cronin enhancement. The main source of enhanced hadron production at p_T midrange is mainly partonic scattering at the initial impact and multiple interactions in nuclear matter [9]. Comparison of R_{AA} between d+Au and A+A collisions can be seen in Figure 1.7. In Au+Au collisions we can observe suppression, but in d+Au enhancement of particle production.

There is also a second possibility to describe influence of the medium on particle production. We can compare collisions with different impact parameters: central and peripheral collisions. For this purpose nuclear modification factor R_{CP} is defined:

$$R_{CP}(y, p_T) = \frac{\langle N_{coll,cent} \rangle}{\langle N_{coll,per} \rangle} \frac{\mathrm{d}^2 N_{cent}/\mathrm{d}y\mathrm{d}p_T}{\mathrm{d}^2 N_{per}/\mathrm{d}y\mathrm{d}p_T} \tag{1.4}$$

R_{CP} is usually used if data from p+p collisions are not at disposal at the same $\sqrt{s_{NN}}$ as A+A collision or they have too small statistics.

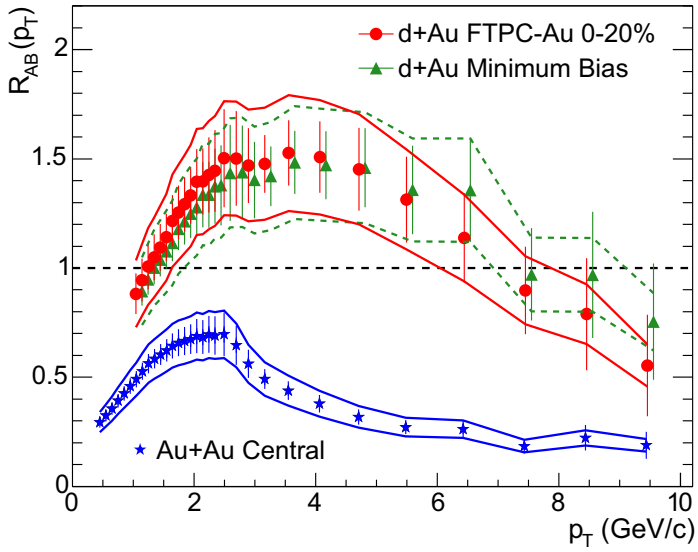

Figure 1.7: The nuclear modification factor R_{AB} for minimum bias (triangles) and central d+Au collisions (circles), and central Au+Au collisions (stars) measured by the STAR experiment at RHIC [10].

Chapter 2

STAR Experiment

2.1 RHIC

The Relativistic Heavy Ion Collider (RHIC), shown in Figure 2.1, is the second largest collider in the world currently in operation. It is the first device capable of colliding heavy ions which has begun operation in 2000. RHIC is located at Brookhaven National Laboratory (BNL) on the Long Island near New York. RHIC was built in order to collide relativistic protons and heavy ions to study formation of quark-gluon plasma and spin physics by experiments with polarized protons. RHIC is able to collide various ion species, as well as enables study of asymmetric collisions - beams with unequal masses. So far following systems were measured: p+p, d+Au, ^{3}He+Au, Au+Au, Cu+Cu, Cu+Au, U+U. The maximum energy of beam for collisions of heavy nuclei is $\sqrt{s_{NN}} = 200$ GeV per nucleon pair and $\sqrt{s} = 500$ GeV for p+p collisions. For Beam Energy Scan are used different energies of the Au+Au collisions. The range of energy is from $\sqrt{s_{NN}} = 7.7$ to 39 GeV and with larger data set at 62, 130 and 200 GeV [12].

RHIC consists of two separated storage rings (yellow and blue beam line) of superconducting magnets, that are 3.8 km long in circumference with six intersection points located on straight sections between 6 arc sections. The superconducting magnets include various types: dipoles, quadrupoles and sextupoles, that are utilized to bend, focus and steer the beams. The total number of magnets is 1740 and they are cooled to temperature of less than 4.6 K. For accelerating heavy ions to the maximum energy it is necessary to utilize accelerator complex. Firstly heavy ions are accelerated to energy of 2 MeV/nucleon by the Electron Beam Ion Source [11]. Ions continue to the Booster Synchrotron, where they are accelerated to 95 MeV/nucleon and then delivered to the AGS where they reach energy up to 10.8 GeV/nucleon. Finally the ions are injected to RHIC via the Beam Transfer Line. Before each section, heavy ions are always partially stripped of electrons. Polarized protons start accelerating at 200 MeV Linac and then they undergo the same accelerating scheme as heavy ions [13]. During physical run, RHIC stores 111 bunches with intensity of 10^9 ions in each storage ring. Initially, RHIC was used for four independent experiments: BRAHMS, PHOBOS, PHENIX and STAR. BRAHMS and PHOBOS already successfully completed their experimental program and only STAR and PHENIX are currently in operation.

2.2 STAR detector

The STAR detector [15] (Solenoidal Tracker at RHIC), depicted in Figure 2.2, was built in order to study behavior and properties of strongly interacting QCD matter produced at high temperatures and energy densities produced in high energy heavy-ion collisions. It is able to observe and identify the majority of particles produced in a collision. The STAR detector is located at intersection point that is at the 6'o clock position of the RHIC collider. It has a shape of cylinder with detector layers around the beam axis. Most of the detectors are placed at mid-rapidity and have full azimuthal angle coverage. The STAR detector is 6.85 meters long and the radius is 7.32 meters. Around the whole detector is a large solenoidal

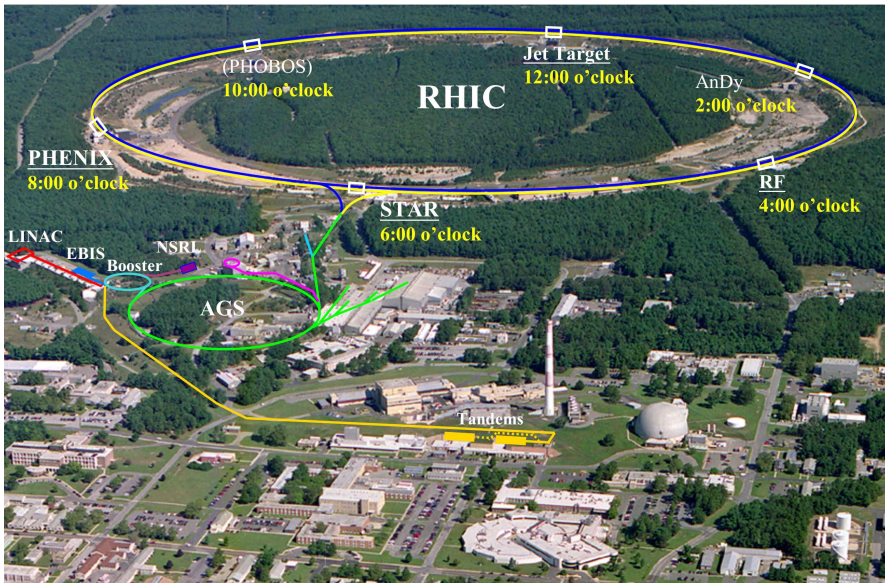

Figure 2.1: Relativistic Heavy Ion Collider [14].

magnet with magnetic field of 0.5 T. STAR consists of several types of detectors and subsystems which allow tracking, triggering, particle identification and measurement of deposited energy of particles. These detectors are: Time Projection Chamber (TPC), Time Of Flight detector (TOF), Barrel ElectroMagnetic Calorimeter (BEMC), Vertex Position Detector (VPD), Beam Beam Counter (BBC), Muon Telescope Detector (MTD), Heavy Flavor Tacker (HFT), Zero Degree Calorimeter (ZDC), Silicon Strip Detector (SSD) and others. The main purpose of the STAR experiment is to measure with large spatial acceptance hadrons, leptons and photons arising from proton-proton or heavy-ion collisions.

2.2.1 Time projection chamber

The Time projection chamber (TPC) [17] is the largest detector of STAR. Its main function is track reconstruction of charged particles on the basis of the measurement of specific ionization energy loss and curvature of tracks in the magnetic field of 0.5 T parallel to the beam pipe. The TPC has a cylindrical shape and length 4.2 meters, inner radius is 50 cm and outer radius is 200 cm. It covers full azimuthal angle 2π with pseudorapidity $|\eta| \leq 1$. The overall tracking efficiency of the TPC is 80-90 % at track $p_T > 1$ GeV/c and the systematic error of track reconstruction is about 4-5%. It is filled with P10 gas regulated at the pressure of 2 mbar larger than atmospheric pressure. Gas P10 is a mixture of two gases: argon (90%) and methane (10%). In order to obtain good detection performance, gas should not influence yield or velocity of electrons. Inert gas does not decelerate electrons and does not capture them and organic gas prevents propagation of UV rays. The TPC consists of a central cathode and two anodes located at sides. The whole detector is divided into two parts, where in between is a thin carbon coated annulus membrane - High Voltage membrane with 28 kV. The function of this membrane is to form a uniform longitudinal electric field that is parallel to the beam pipe and its value is 135 V/cm. At both ends of the TPC there is a readout system based on multi-wire proportional chambers (MWPC). The end caps contain 12 sectors of anode pads. A scheme of the TPC is depicted in Figure 2.3.

A charged particle going through the TPC ionizes the gas around its track and releases electrons from gas molecules. These kicked out free electrons are accelerated in the electric field and drift with the constant velocity to the anode end caps. Before electrons reach end of the TPC, their velocity is increased by electric field to allow ionization of gas and produce another electrons in the avalanche. The average velocity of an electron is referred to as a drift velocity. The average number of produced electrons

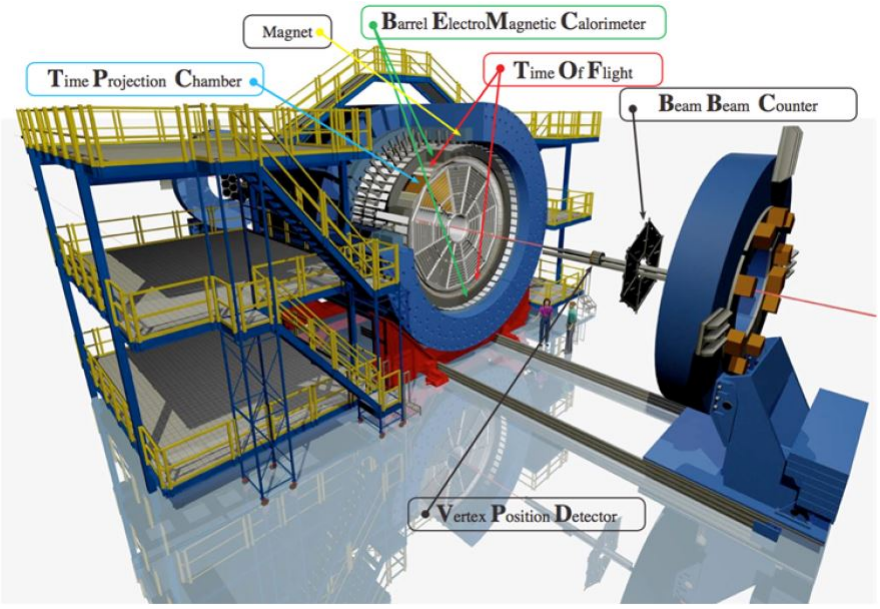

Figure 2.2: STAR detector [16].

is proportional to the energy released in the detector (or energy that particle loses in the TPC). Then the signal of the electron is amplified and recorded. Wires of MWPC are formed into grid, which allows us to determine two coordinates (x,y) of each part of a track. The longitudinal coordinate z is obtained from the time of drift. This means that the TPC is able to reconstruct tracks in 3 dimensions, therefore we can obtain important information about trajectory of each charged particle passing through the TPC.

To calculate energy loss of a particle in material, the Bethe-Bloch formula is used:

$$\frac{dE}{dx} = 4\pi N_A r_e^2 m_e c^2 z^2 \frac{Z}{A}\frac{1}{\beta^2}\left(\frac{1}{2}\ln\frac{2m_e c^2\beta^2\gamma^2 T_{max}}{I^2} - \beta^2 - \frac{\delta}{2}\right) \tag{2.1}$$

where N_A is the Avogadro number, r_e classical electron radius, m mass of particle that loses energy, c speed of light in vacuum, ρ density of material, Z proton number, A nucleon number, W_{max} maximum energy transfer in a single collision, I mean excitation energy and δ density correction. This formula allows us to identify particles as can be seen in Figure 2.4 where the $\frac{dE}{dx}$ is a function of momentum of particles measured by the STAR TPC. Momentum of particles is computed from a curvature of the particle track in the magnetic field.

2.2.2 Time of flight

The Time of Flight detector (TOF) of STAR [13] is designed for improvement of direct identification of hadrons. It is located between the TPC and the BEMC and covers full azimuthal angle and pseudorapidity $|\eta| \leq 1$. The TOF is based on Multi-gap Resistive Plate Chamber (MRPC) technology. The MRPC module is in each tray and there are 120 trays included in the TOF. The TOF detector is activated by a VPD (Vertex position detector) and with assistance of momentum obtained from the TPC improves precision of particle identification. The time resolution of the TOF is high - 100 ps and allows the TOF effectively distinguish electrons from heavier hadrons with a low momentum. Thus it is possible to identify pions and protons to 7-8 GeV/c, kaons to 3 GeV/c and electrons in the interval of 0.15 - 4 GeV/c [18]. High momentum particles are identified by other detectors, e.g. the BEMC. The principle of particle determination or respectively its mass is as follows: the time of flight particles traversing through detector is measured. The starting time t_0 is recorded by the VPD and the TOF measures the end time

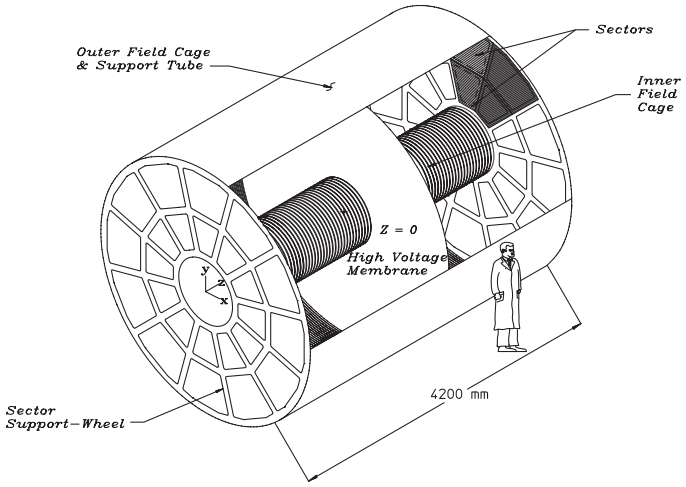

Figure 2.3: A schematic view of a Time Projection Chamber [17].

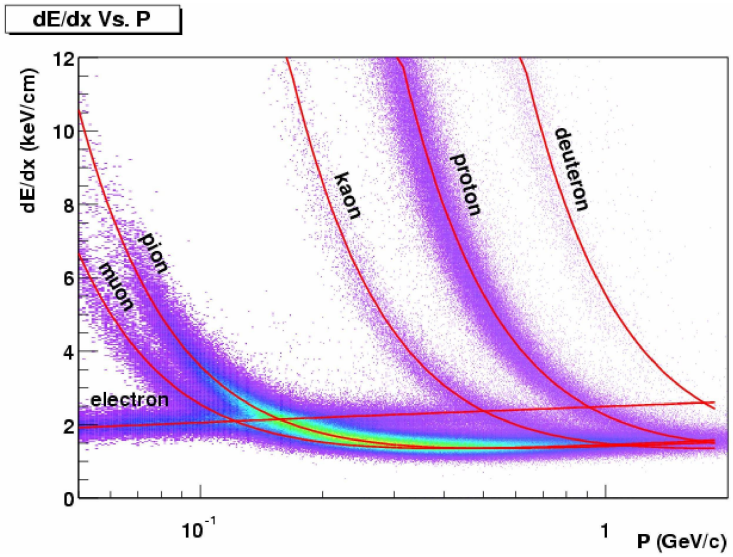

Figure 2.4: The result of energy loss dE/dx distribution measurement in TPC STAR as a function of the transverse momentum p_T. Measurement is used for particle identification [17].

t_1. From these measurements we can obtain the time-of-flight interval $\Delta t = t_1 - t_0$. Then using the interval Δt and the length s of particle track acquired from the TPC, the value of inverse velocity is computed:

$$\frac{1}{\beta} = \frac{c\Delta t}{s}. \tag{2.2}$$

Finally from the momentum of the particle and its velocity β we are able to calculate mass according to the formula:

$$m = p\sqrt{\left(\frac{1}{\beta^2}\right)^2 - 1} \tag{2.3}$$

2.2.3 Barrel Electromagnetic calorimeter

The STAR Barrel Electromagnetic Calorimeter (BEMC) [19] is located between the TOF detector and the solenoidal magnet. Its distance from the beam pipe is 223.5 cm. It covers full azimuthal angle and has pseudorapidity coverage $|\eta| \leq 1$. Its purpose is to measure energy deposition of high momentum particles such as photons, electrons and hadrons. The BEMC consists of 120 calorimetric modules (in azimuthal angle), each segmented into 40 towers (in pseudorapidity). A view of the BEMC module is illustrated on Figure 2.5. The total number of towers in the BEMC is 4800, where the effective size of the tower as the BEMC resolution is 0.05 x 0.05 = $\Delta\phi$ x $\Delta\eta$.

The BEMC is a sampling calorimeter and the core of each calorimeter module comprises of a lead-scintilator stack and shower maximum detectors. It is made of 41 layers, where 21 layers are active scintillators that measure deposited energy of traversing charged particles and between them there are lead absorber plates. As a charged particle traverses these lead layers it produces an electromagnetic shower. This shower is detected by scintillators that convert energy of particle from the shower into the light and according to intensity of light we are able to determine amount of deposited energy of the particle. The actual deposited energy in the calorimeter depends on the type of particle and thus allows its identification.

The thickness of the BEMC detector is approximately 20 radiation lengths for an electron. The radiation length is defined as a distance that a high energy electron has to pass to lose $1/e$ of its original energy by radiation referred to as bremsstrahlung. Energy-momentum ratio E/p for high energy electron is 1. Due to this, it is expected that electrons and photons are completely stopped in the BEMC because they lose their whole kinetic energy. In contrast the cross section of hadrons with lead is much smaller in comparison to electrons. This means that hadrons are less ionizing particles $E/p < 1$. They do not lose their whole energy in the detector and they pass through it. Consequently, it is possible to distinguish high energy electrons form hadrons. By measuring deposited energy of high energy particles in the BEMC and by detecting their produced showers, we are able to study high p_T processes as leading hadrons and jets.

2.2.4 Beam Beam Counter

There are two Beam Beam Counters (BBCs) on both sides of the STAR detector. They are located 3.5 m before the intersection point in STAR and surround the beam pipe. They cover pseudorapidity in the interval of $2.1 < |\eta| < 5.0$. The main function of the BBC is to locate the position of a collisional vertex and determine collision centrality. The BBC consists of two rings of hexagonal scintilators.

2.2.5 Vertex Position Detector

The capability of the Vertex Position Detector (VPD) is determination of z position of the primary vertex - the point of collision. The VPD measures the start time for the TOF. It covers pseudorapidity $4.24 < |\eta| < 5.0$. There are two VPDs (West and East) located on both sides of STAR in the distance of 5 m from the intersection point and they surround the beam pipe. The VPD consists of 19 detectors, each of them composed of a lead converter followed by a fast plastic scintilator that is read out by a photomultiplier tube (PMT).

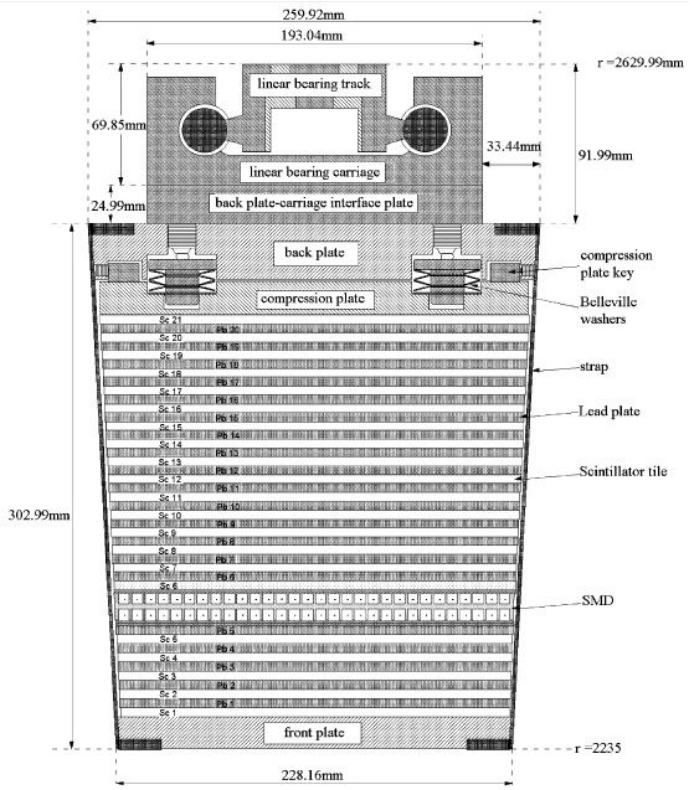

Figure 2.5: A schematic view of the BEMC module [19].

2.2.6 Muon Telescope Detector

The Muon Telescope Detector (MTD) [20] enables detection of muon pairs from QGP thermal radiation, quarkonia, light vector mesons and heavy flavor through semileptonic decays. These processes can be studied also through photons or electrons, but in comparison to muons they have larger background. The MTD is situated on the top of the solenoidal magnet. Its location is convenient because there is very low hadronic background and noise. Muons are more penetrating than hadrons therefore mainly muons pass through the whole STAR and reach the MTD. For this reason we are able to distinguish and observe different Υ states. The MTD covers only 45 % of the full azimuth, its pseudorapidity coverage is $|\eta| < 0.5$ and its radius is 4 m. In the MTD there is installed a similar detection system and technology - MRPC as in the TOF.

2.2.7 Heavy Flavor Tracker

The main function of a new Heavy Flavor Tracker (HFT) [21] is to precisely determine the secondary vertex of mesons that rapidly decay and contain heavy quarks, like D^0 or B^0. The HFT is a system of three detectors: a silicon pixel detector (SPD), an intermediate silicon tracker (IST) and a silicon strip detector (SSD). The HFT improves analysis of heavy flavor and it is located in the center of STAR. The minimal radius of the HFT is only 2.5 cm and hence it tightly surrounds the beam pipe that had to be thiner than in another place at RHIC. The HFT is the first detector of STAR through which a particle passes.

2.2.8 Trigger system

In a typical Au+Au collision at $\sqrt{s_{NN}} = 200$ GeV, a large amount of data is produced, but technically it is not possible to analyze and register all data from all events, because the operating speed of STAR detectors is smaller than collision rate of RHIC. Therefore we need to reduce the rate of readout and for this function a trigger system is used.

The STAR trigger system is divided into four Levels: 0, 1, 2, 3 [22] . It uses information measured by fast detectors and based on knowledge of this decides whether a given event is suitable to trigger on and to be registered. The main fast detectors used for triggering are ZDC, VPD, BBC, TOF and BEMC. Level 0 consists of ZDC, VPD and BBC. Each collision is monitored by detectors of Level 0 that govern if the collision fulfills defined requirements or not. The capability of the ZDC is monitoring the luminosity and on the basis of detected number of spectators to determine centrality of the collision.

If the event is evaluated positively then the Level 1 and 2 starts. They are more time-consuming due to complex analysis of the trigger data. The main aim of Level 1 and 2 is to determine if the event fulfils more finely grained criteria. Simultaneously digitalization process and data transmission phase of the TPC take place and they can be aborted by these two Levels if data do not comply. Level 3 represents on-line analysis preformed by large CPU farms. Produced data are reduced and stored by a Data Acquisition System (DAQ) on tapes using technology of High Performance Storage System (HPSS).

Chapter 3

Jets

3.1 Definition of a jet

One possibility how to study the strong interaction and properties of QGP is observation and analysis of jets, which are experimental signatures of quarks and gluons. Jets are one of the most important probe of QGP and they are used in hard scattering and hadronisation studies. Jets are narrow conical sprays of particles, which are produced in the hard scattering during the initial stage of ultra-relativistic proton or heavy-ion collisions. In the early stage of the collision partons from incoming nuclei scatter and recede form each other. The scattered parton has a large amount of kinetic energy that is gradually lost by gluon radiation and production of quark-antiquark pairs moving along the trajectory of the original leading parton. It is referred to as a fragmentation. New partons are colour charged and due to color confinement they cannot remain free. Instead they combine together and form colourless hadrons, therefore this process is called hadronization. It implies that the jet is a collimated shower of particles, mainly hadrons (mostly pions and protons) and posses same kinematic properties as the original parton. Jets are always produced in pairs of opposite direction ($\Delta\phi \approx \pi$) in their centre of mass reference frame, because an emerging quark and antiquark that are produced during hadronisation process have to conserve momentum. Such events are called di-jet events. They are the most common in p+p collisions. But also sometimes a quark radiates a gluon before hadronisation. The gluon fragments producing a new jet. Therefore we can also observe three-jet, four-jet... events.
Proper reconstruction, comprehensive analysis and thorough physical interpretation of jets allow to access early stages of the collision and obtain useful information about medium created in the collision area, which helps for better understanding of QCD laws. QCD calculations and simulations are able to describe jet production in p+p collisions satisfactory, but on the other hand in heavy-ion collisions more detailed studies are required.

3.1.1 Jet quenching

At the initial stage of a heavy-ion collision when hard scattering occurs, two partons can interact with each other. They recoil, fragment and hadronise into jets, back-to-back shower of hadrons. If high p_T parton (> 2 GeV), called a hard probe propagates through strongly interacting dense medium - QGP, it loses energy by two mechanisms: elastic and inelastic scatterings with the surrounding medium constituents, in other words by collisional and radiative energy loss. After subsequent hadronization the quantity of observed high p_T hadrons might be smaller, because they can be absorbed by medium or their energy strongly attenuated. This effect might cause modification of the spectrum of jets and their properties. This phenomenon is referred to as a jet quenching and its first evidence has been observed in $\sqrt{s_{NN}}$ = 200 GeV Au+Au collisions at RHIC [23] and later at the LHC [24]. Jet quenching provides direct information on the QCD matter and its thermodynamical properties such as temperature, energy or

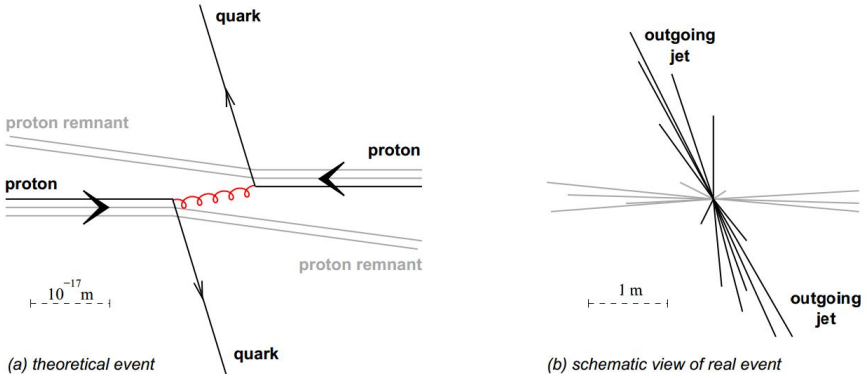

Figure 3.1: (a) Theoretical interpretation of p+p collision, (b) schematic representation of real event [27].

particle densities and transport properties (viscosity, diffusivity and conductivity coefficients) that can be obtained by comparing the jet production in heavy-ion collisions to proton-proton collisions [25]. This phenomenon is depicted in Figure 3.2. On the left-hand side of the figure there is a di-jet event arising from the p+p collision, in which the dense and hot medium is not created contrary to the right part of the figure, where the medium is created and jets are modified and eventually quenched. In the p+p collision the size of both opposite jets is almost the same, but in a heavy-ion collision, the size of a jet arising from the edge of the collision region is larger than size of the opposite jet that is suppressed by medium. We can see that not only presence of medium change the properties of a jet, but also the position of its emergence and quantity of medium.

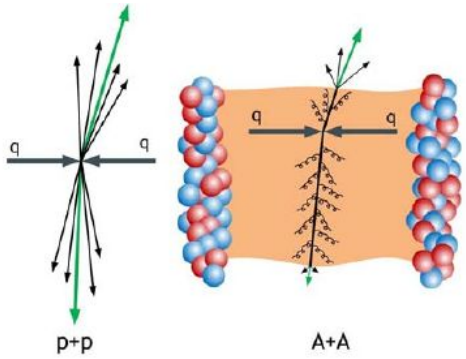

Figure 3.2: Jet quenching [26].

3.2 Jet reconstruction

For jet reconstruction several types of jet finding algorithms were developed. Jet algorithm is a set of procedures and instructions that aim for identifying jets as the observable counterparts of the perturbative concept of partons. Their right definition is crucial for comparison of experimental analysis with theory. They are widely used in jet analysis in experiments at the LHC or RHIC.

The main goal of jet algorithms is to cluster a set of charged tracks and neutral towers measured by detectors into jets in $\eta - \phi$ plane. At the beginning, the algorithm selects a set of particles, which are typically emitted close to each other in space. At experimental level these particles are hadrons and

partons in a pQCD calculation or simulation level. During the jet analysis, each jet is assigned a four-momentum $p = (E, \vec{p}) = \sum(E^i, p_x^i, p_y^i, p_z^i)$ and transverse momentum p_T. The jet algorithm combines momenta of measured particles to form the momentum of a jet. The momentum addition rule is called the recombination scheme.

3.3 Attributes of ideal jet algorithm

An ideal jet algorithm has to fulfil several theoretical and experimental attributes, because there is no exact solution or definition of a jet. The result of a jet usually depends on a type of algorithm used. To get a correct result or at least a result, which converges to the right solution and complies with the demands of the study, every reliable jet algorithm has to fulfil following criteria [28]:

- Full specification: jet selection process, jet kinematic variables, specifications for clustering, energy and angle definition, and all details of jet splitting and merging should be clearly and completely defined.
- Detector independence: application of jet algorithm should provide similar results on various types of detectors, which differ from each other in size, cell type, detector segmentation, energy response or resolution.
- Order independence: algorithm behaves equally in pQCD calculations, simulations and data reconstruction (parton, particle and detector level).
- Infrared safety: algorithm should find a solution which is insensitive to any soft radiation in the event - any radiated soft gluons or products of hadronization will not influence existence, number or shape of a jet. Figure 3.3 illustrates infrared safety of a jet algorithm.

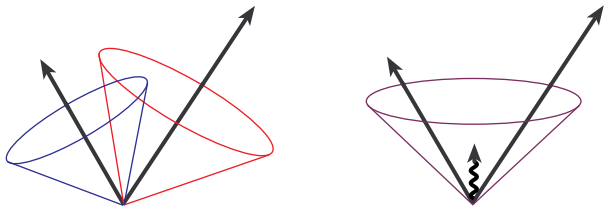

Figure 3.3: Infrared safety of a jet algorithm [28].

- Collinear safety: Let us assume two particles moving together, which mutual distance is short and have smaller energy than other particles in arising jet. They can be detected together in one tower of the detector. In this case detector considers them as one signal and the final jet could be reconstructed incorrectly or not at all. If the jet algorithm is not influenced by this effect, this characteristic is denoted collinear safety.
- Maximal reconstruction efficiency - all relevant jets are reconstructed
- Efficient use of computer resources and time: Because of the enormous amount of data, especially in heavy-ion collisions, the jet algorithm should provide jet identification with a reasonable computing time.

3.4 Classes of jet algorithms

During the years of the jet study there has been a demand to the jet algorithms, which can reconstruct jets fast with high precision and implement attributes mentioned above. Many types of jet algorithms

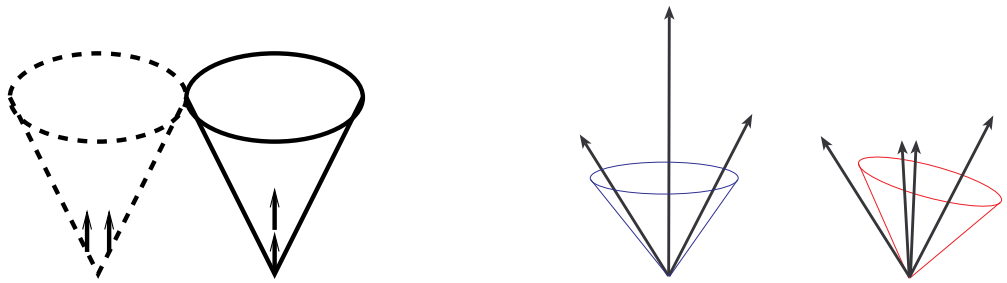

Figure 3.4: Collinear safety of a jet alorithm [28]

were developed, which differ slightly form each other in some attributes and in their scheme of jet finding, These attributes are: sequence of steps to find a jet, initial energy and momentum parameters, collinear and infrared safety, boundary sensitivity and sensitivity to non-perturbative effects, e.g. hadronisation and underlying event contamination. According to the selection of starting particle, jet algorithms can be classified to seedless and seeded that start by choosing the most energetic particle in the event, which is called a seed. The seedless jet algorithm looks for all stable solutions of jet from all entries without choice of any seed. Moreover, jet algorithms can be divided into two groups: cone and sequential recombination.

3.4.1 Cone Algorithms

Seed cone Algorithm

The cone algorithm approximates particles of a jet into a cone around a direction of dominant energy flow. The vertex of the cone is in the location of decay of parent particle. The main goal of this algorithm is to look for a stable cone. The cone algorithm starts by drawing a circle of a specific radius $R = \sqrt{\Delta\eta^2 + \Delta\phi^2}$ (where R is a radius of a cone, η is pseudorapidity and ϕ is azimuthal angle) in $\eta \times \phi$ plane around the highest p_T or the most energetic particle of the collision, which is called seed. Then the total transverse momentum and energy of a jet is computed including contributions from all particles located inside the cone. This leads to formation of a new point in $\eta \times \phi$ plane which is subsequently used as the center of a new trial cone. This iteration process runs until the stable cone is found and everything inside the cone is proclaimed as a jet. The jet is proclaimed as a stable one if direction of the resulting jet (sum of momentum vectors of all particles inside a jet) is identical with the axis of the starting particle. But if the difference between axis of resulting jet and starting particle is larger than determined criterion then it is necessary to recalculate the momentum of founded trial cone. A new cone is created with the same radius R and compared to the the axis of previous cone again.

After iteration process of stabilization of jets, a procedure of splitting or merging is needed to be run, because areas of jets can overlap. Two jets will be merged if the percentage of shared transverse energy of the lower p_T jet is greater than 50%, otherwise they are split [28]. The cone algorithm behaves as a collinear, but its disadvantage is infrared unsafe. But on the other hand it is very fast and simple.

SISCone algorithm

The seedless infrared safe algorithm (SISCone) is the next cone algorithm, but in comparison to cone, SISCone is infrared and collinear safe. The main aim of this algorithm is also to identify all circular enclosures - cones and test their stability. Its basic steps are described and depicted in Figure 3.5 as follows [32]:

1. A circle of radius R around a point, which represents a particle is put into an event in $\eta \times \phi$ plane.
2. The circle is moved in a random direction and until the edge of the circle hits a point outside.
3. The circle is rotated around the boundary point until another one touches the edge of the circle.

4. The procedure above is repeated until all points in nearby area of starting points are included.
5. All particles defined by pairs of edge points form a jet.

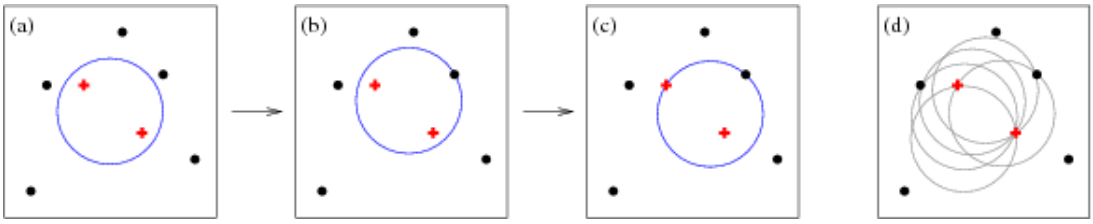

Figure 3.5: Scheme of the SISCone algorithm [32].

3.4.2 Sequential recombination algorithms

The sequential recombination algorithms have become in the last years the main tool for analysing data from high energy collisions. In comparison to the cone algorithms, sequential recombination algorithms are based on specific selection of a starting particle and then sequentially add other particles that are close enough to the arising jet. Their advantage is that they collect the most of the particles that are radiated from an original parton so the efficiency of reconstruction is high [31]. But their disadvantage is slowness in high multiplicity environment.

This class of jet algorithms starts with a list of preclusters and empty list of jets. Preclusters are tracks and towers measured by a detector. Initially a vector $(E, \vec{p} = E(1, \cos\phi \sin\theta, \sin\phi \sin\theta, \cos\theta))$ is assigned to each precluster, where E is the energy of the precluster, ϕ is the azimuthal angle and θ is the polar angle with respect to the beam axis. Then the square of transverse momentum p_T^2 is calculated for each precluster
In order to find final jets from preclusters, algorithm carries out several steps outlined bellow [28]:

1. The clustering algorithm begins with a definition of distances d_i and d_{ij}:

   - For each precluster i in the list, define distance from the beam

   $$d_i = p_{T,i}^{2n} \tag{3.1}$$

   For each pair (i, j) of preclustes $(i \neq j)$, define distance between i and j

   $$d_{ij} = min(p_{T,i}^{2n}, p_{T,j}^{2n}) \frac{\Delta_{ij}^2}{D^2} \tag{3.2}$$

   where $\Delta^2 = (y_i - y_j)^2 + (\phi_i - \phi_j)^2$ and p_{Ti}, y_i, ϕ_i are respectively the transverse momentum, rapidity and azimuth of precluster i. For each particle or tower the transverse momentum is defined as:

   $$p_{Ti} = \frac{E_i}{c} \sin\theta_i \tag{3.3}$$

   where θ_i is an angle between the direction of a particle and the beam of colliding nucleons. R is a radius parameter that represents size of a jet and the minimum distance between two pairs of jets i, j. Simply, R is a minimal radius of a jet and typical value used in data analysis is 0.2 to 1.0. Parameter n governs the relative power of the transverse momentum versus geometrical (Δ_{ij}) scales. Different values of $n \in -1, 0, 1$ correspond to three clustering algorithms: k_T, $anti - k_T$ and Cambridge/Aachen, which will be discussed later.

2. After computation of all distances d_i, d_{ij} and excluding values below a jet resolution threshold d_{cut}, the minimum of them is found and labeled as d_{min}.

3. The next step of algorithm depends on attribute of d_{min}:

   - If d_{min} is a d_{ij}, preclusters i and j are removed from the list and replaced by a new merged precluster: $p_{ij} = p_i + p_j$ and $E_{ij} = E_i + E_j$
   - If d_{min} is a d_i, the corresponding precluster can not be merged and it is removed form the list of preclusters and add it to the list of jets.

4. If any preclusters remain, values d_{min} are calculated again and the whole process of jet finding is repeated. It can happen that a jet overlaps with another one, then the common area is assigned to a jet with higher or lower transverse momentum according to the algorithm used.

In general, all jet clustering algorithms are infrared and collinear safe.
As was said before, there are three most commonly used clustering algorithms: k_T, anti-k_T and Cambridge-Aachen. They differ from each other in calculation of distance between particles. The main characteristics of clustering algorithms are as follows:

k_T algorithm
The k_T algorithm recombines first particles with low p_T close to each other in space. It implies its sensitivity to soft background because it prefers soft particles. Use of the k_T algorithm in heavy-ion collisions might cause problems because if we compare jet reconstruction in a hard event without background to an event with added soft particles, resulting jets will be different. Not only the energy of jets is higher due to energy of soft background, but also jet shapes are changed and less regular. This feature is called back reaction. Therefore the k_T algorithm is usually used for estimation of background. Scheme of k_T algorithm is depicted in Figure 3.6.

$anti - k_t$ algorithm
The anti-k_T inclusive jet finding algorithm belongs to a class of jet clustering algorithms, where the power of the energy scale is negative. It acts as an idealized cone algorithm [33], because reconstructed jet shapes are regular and quite circular. Unlike the k_T algorithm, the anti-k_T algorithm is resilient to the soft background, since it clusters first particles with the highest p_T. Soft particles are connected to hard one before recombination among themselves. This leads to the high suppression of the effect of the back reaction. The anti-k_T algorithm is currently the most used for jet analysis.

Cambridge/Aachen algorithm
The power of energy is 0 in this algorithm. It means that momentum of particles is not taken into consideration at all, therefore recombination is based only on spatial separation.

It is also important to mention, that each algorithm has specific computing time. Comparison of speed, infrared and collinear safety of jet algorithms is given in Table 3.1. We can see that the fastest algorithm is the Cone, but in comparison to other algorithms its disadvantage is infrared and collinear unsafety. SISCone and clustering algorithms are slower, but they are effective and reliable in data analysis. Computation time of jet algorithms is compared in Figure 3.7.

3.5 Jet areas

Jet area is a measure of susceptibility of a jet to soft radiation (underlying event, pileup), that is uniformly distributed in rapidity and azimuth around the jet. Jet areas are used for subtraction of the jet contamination by soft radiation. There are two main definitions of jet area: passive and active [34]:

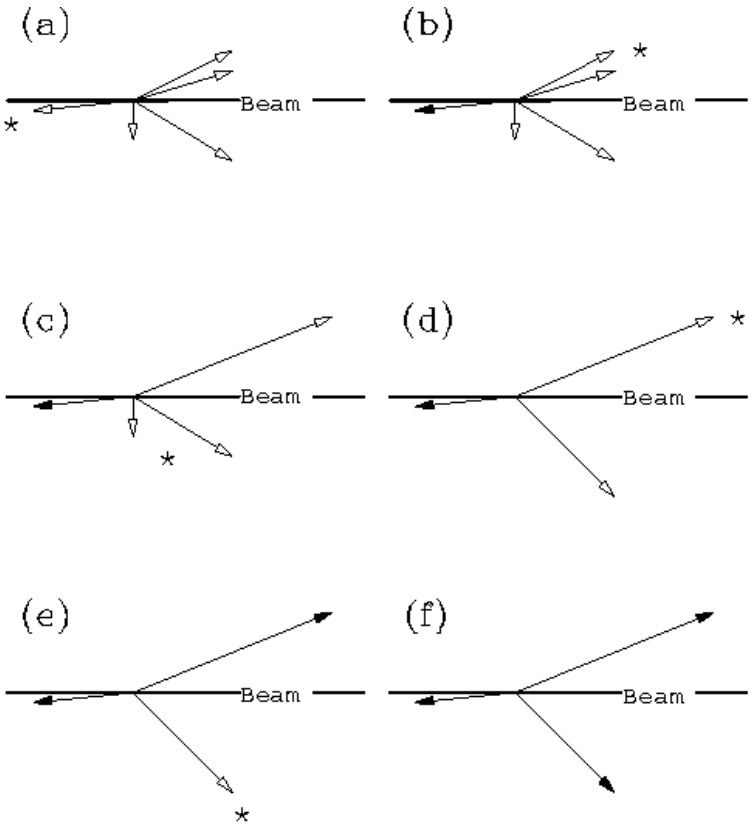

Figure 3.6: Scheme of k_T algorithm [28]

Algorithm	Speed	Infrared safety	Collinear safety
Cone	N	no	no
SISCone	$N^{3/2}$	yes	yes
k_T	$N \ln N$	yes	yes
anti-k_T	$N \ln N$	yes	yes
Cambridge-Aachen	$N \ln N$	yes	yes

Table 3.1: Comparison of speed, infrared and collinear safety of jet algorithms [30].

- **Passive area**: it is a measure of the susceptibility of the jet to pointlike radiation. A single ghost particle is added to the event. Then the region in which a jet clusters with a single ghost is defined as a passive area. The passive area geometrically equals to πR^2.
- **Active area**: a dense coverage of soft ghosts g_i each with an infinitesimal p_T, randomly distributed in rapidity and azimuth with density distribution per unit area ν_g is added to the event. Ghosts might cluster with each other and also with hard particles. Because of infrared insensitivity of jet algorithm, the addition of ghosts does not influence the shape or the momenta of the final jet. The number of ghosts in a jet is used as a measure of jet area. In comparison to the passive area, which has shape of a circle, the structure of the active area is more complicated. In Figure 3.8 different area structures of various jet algorithms can be seen.

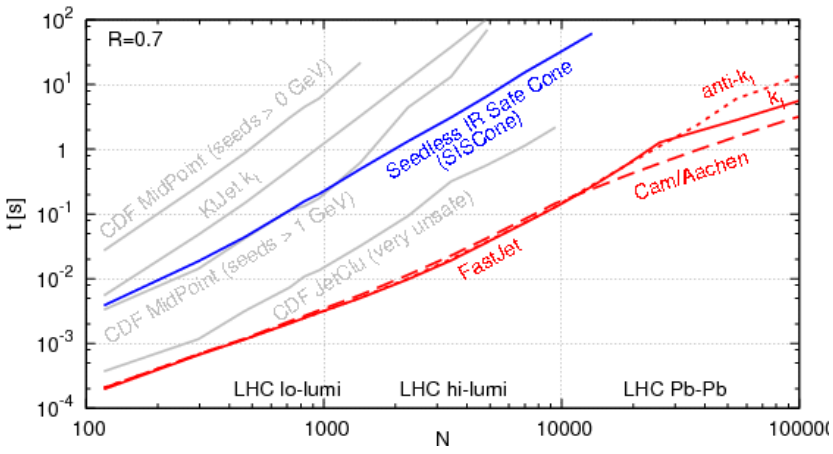

Figure 3.7: Timings for the clustering of a simulated 50 GeV di-jet event with Pythia) [30].

3.6 FastJet

The FastJet package [36] is a powerful software package used for jet analysis . It has been written in C++ by Matteo Cacciari, Gavin Salam and Gregory Soyez and includes a broad range of jet analysis tools. Fastjet provides fast implementations of all most used jet sequential recombination algorithms such as k_T, anti-k_T and Cambridge/Aachen jet finders. It can be extended by SISCone and other cone algorithms via plugin. FastJet also includes tools for calculating jet areas, performing background estimation of pileup and underlying events, background subtraction and for jet substructure analyses [36].

3.7 Jet background

A critical issue of each jet analysis is the background, mainly in high multiplicity environment of heavy-ion collisions. A large amount of soft (low p_T) particles is produced which do not originate from the initial hard scattering and during jet reconstruction they might end up in a jet and modify jet p_T [30]. These low p_T particles are roughly uniformly distributed in η-ϕ space and they originate in several sources [29]:

- Underlying event - products of interactions between hadron remnants that are produced in heavy-ion collisions. Underlying event also includes multi-parton interactions and initial and final state radiations
- Pileup - multiple nucleon-nucleon interactions created by crossing bunches of particles in an event

To acquire true jet p_T, it is important to subtract soft component of p_T from jets. The process when a background is subtracted from measured jets is called decontamination of a jet and it is carried out after all jets are found. The transverse momentum density of background ρ is estimated by using concept of active jet areas [35] as follows [8]:

$$\rho = \text{median}\left(\frac{p_{T,i}}{A_i}\right) \tag{3.4}$$

where i runs over all reconstructed jets with transverse momentum $p_{T,i}$ and area of jet A_i in the event. For the median jet energy density ρ calculation the k_T algorithm is used for jet finding, because it is infrared safe and more sensitive to soft particles than anti-kt algorithm.

Then an event-by-event correction is provided for each jet with p_T from which the median of jet energy density multiplied by the jet area A is subtracted:

$$p_{T,corr} = p_{T,uncorr} - A\rho \tag{3.5}$$

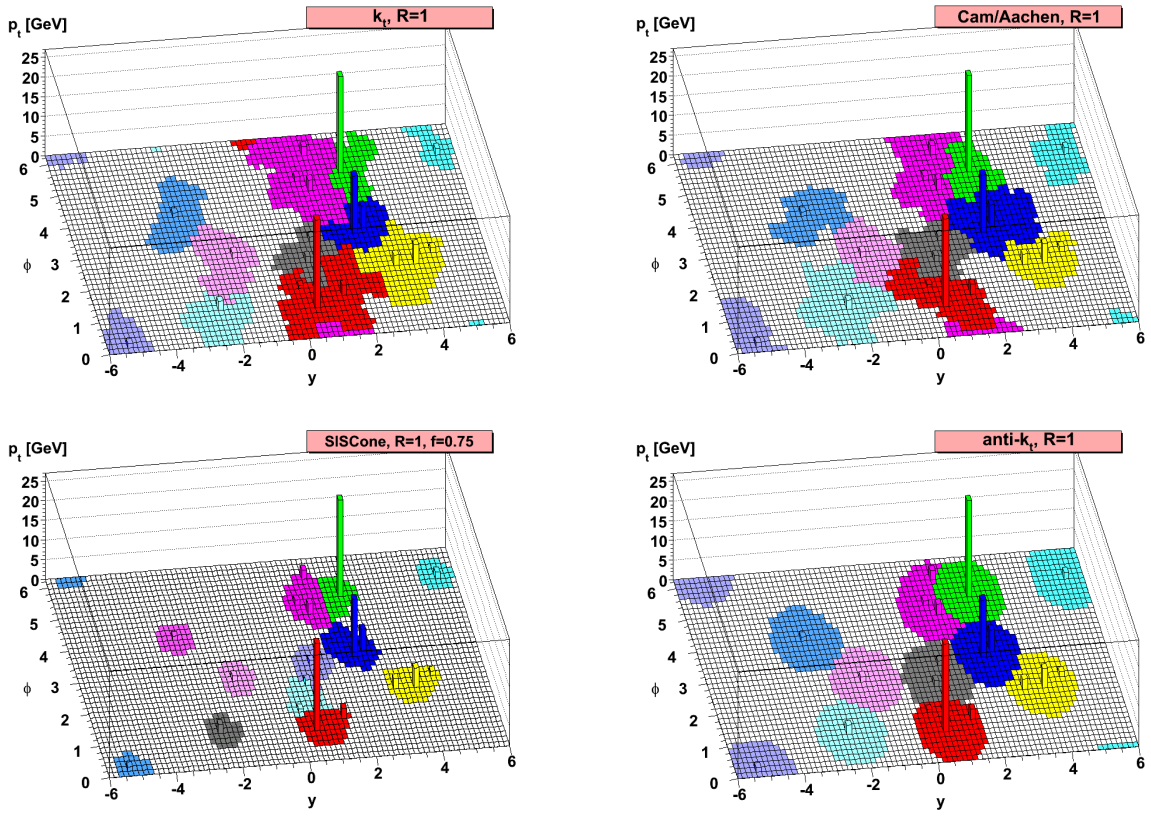

Figure 3.8: Comparison of areas of jet algorithms [33]

3.8 Jet reconstruction at STAR

Jet identification in heavy ion collisions at STAR is extremely challenging task due to background fluctuations which are comparable to signal. Thus jet identification is necessary to be performed on statistical basis. In comparison to jet reconstruction at the LHC, jet identification is simpler, because jets dominate over the background and especially at high p_T it is possible clearly identify a jet. One of the first attempts to perform full jet reconstruction in the environment of heavy-ion collisions was in the analysis of central Au+Au collisions at $\sqrt{s_{NN}}$= 200 GeV from the Run 7 at RHIC. Total number of analysed minimum bias events was 7.6 M. Cut for minimal p_T of jet constituents (tracks and towers) is $p_{T,min} = 0.2$ GeV. Background was subtracted: $p_{T,corr} = p_{T,uncorr} - A\rho$, where A is jet area and background energy density was estimated to $\rho = 75$ GeV [37]. Figure 3.9 shows the jet R_{AA} which is the ratio of the jet production in the most central (0-10%) Au+Au and jet production in p+p collisions (collected in Run 6) scaled by binary collisions. Measured jet R_{AA} for $R = 0.2$ jets is more suppressed than R_{AA} for $R = 0.4$ which is compatible with the unity, within large systematic uncertainties. This fact indicates jet broadening in heavy-ion collisions. There is a difference between algorithms due to their different response to the heavy-ion background. This result is inconclusive and for its improvement higher statistics is necessary to suppress the uncertainties. The right part of Figure 3.9 presents differential cross section for fully reconstructed inclusive jet production in the most central (0-10%) Au+Au collisions.

The STAR Run 11 provides higher statistics, therefore results are more promising. The increase of statistics enables more precise study of the jet R_{AA} as a function of centrality, it also suppresses systematics errors and can provide new insights to background fluctuations in high multiplicity environment of high energy heavy-ion collision. Figure 3.10 presents the first quantitative comparison of jet quenching at

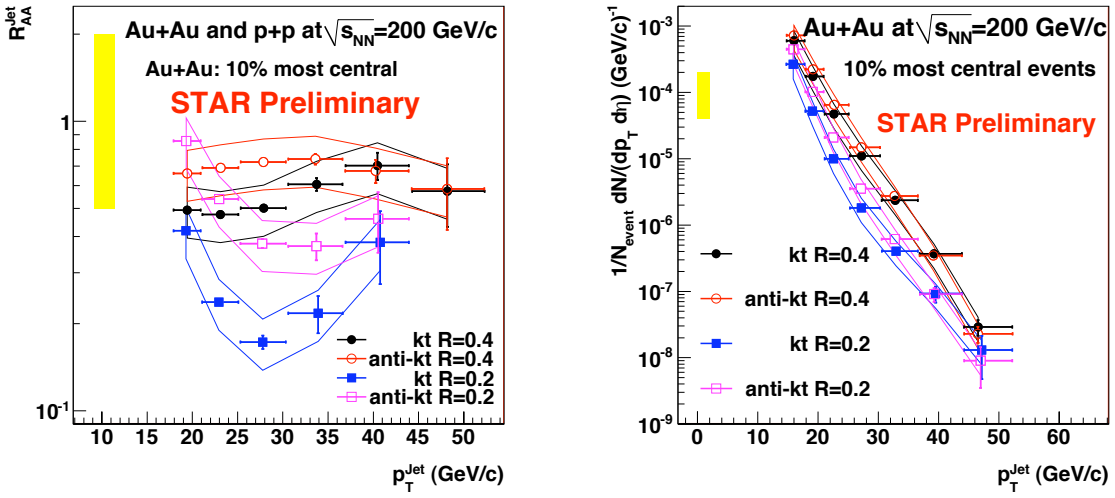

Figure 3.9: Jet R_{AA} (left) and cross section for inclusive jet production (right) in Au+Au collisions at $\sqrt{s_{NN}}$= 200 GeV [37].

RHIC and the LHC. It shows corrected charged semi-inclusive recoil jet spectrum for central 0-10% and peripheral collisions 60-80%. In each event, one trigger hadron was randomly selected from all charged tracks with $p_T > 9$ GeV/c. The cut for maximum track p_T was 30 GeV/c. Jets were reconstructed by the anti-k_T algorithm with the resolution parameter $R = 0.3$ and the jet area cut $A > 0.2$. Jet acceptance is $|\eta| < 1 - R$. Background was subtracted by the method described in the previous section. Figure 3.10 mainly compares the jet nuclear modification factor for central and peripheral Au+Au collisions at $\sqrt{s_{NN}} = 200$ GeV for the jet resolution parameter $R = 0.3$ with the result which was carried out by the ALICE collaboration in Pb+Pb collisions at $\sqrt{s_{NN}} = 2.76$ TeV for $R = 0.4$. The lower panel on the left side shows I_{CP} which is the ratio of central to peripheral distributions. At low p_T the I_{CP} is close to 1. But for $p_{T,jet} > 10$ GeV/c, significant jet yield suppression $I_{CP} \approx 0.2$ can be observed in central collisions. The $p_{T,jet}$ shift between central and peripheral collisions is -6.3 $\pm$ 1.4 GeV/c in the range $10 < p_{T,jet} < 20$ GeV/c The suppression at STAR is larger in comparison to the LHC energy at $\sqrt{s_{NN}} = 2.76$ TeV [39], where the nuclear modification factor I_{AA} is approximately 0.6 and $p_{T,jet}$ shift is about -8 $\pm$ 2 GeV/c in the range $60 < p_{T,jet} < 100$ GeV/c. But it is important to mention that analysis was performed with different measurement techniques, the resolution parameter R at STAR is $R = 0.3$ and ALICE $R = 0.4$.

Figure 3.11 [40] presents corrected spectrum of inclusive charged jets for R=0.2 and 0.3 in central 0-10% Au+Au collisions at $\sqrt{s} = 200$ GeV in Run 11. Jets were reconstructed by the anti-k_T algorithm which used charged tracks from the STAR TPC. Track cut $p_T > 200$ MeV was applied. Jet acceptance is $|\eta| < 1 - R$ and jet area cut for the resolution parameter $R = 0.2$ is $A > 0.09$ and for $R = 0.3$ is $A > 0.2$. Background was subtracted by the method mentioned in the previous section and jet spectrum is corrected to detector effects. This charged jet analysis, whose the author is Jan Rusňák is parallel to the analysis of full jets, which is the main part of this research task. The next chapter describes the beginning of the analysis of full jets and presents uncorrected jet spectra. The main goal of the analysis is to carry out similar analysis as was done by Jan Rusňák, but he works with charged jets and I use full jets (charged tracks + neutral energy towers). The final result of both analyses will be reconstruction of jet spectrum corrected to background fluctuations and detector effects and calculation of jet R_{AA} and all systematics errors.

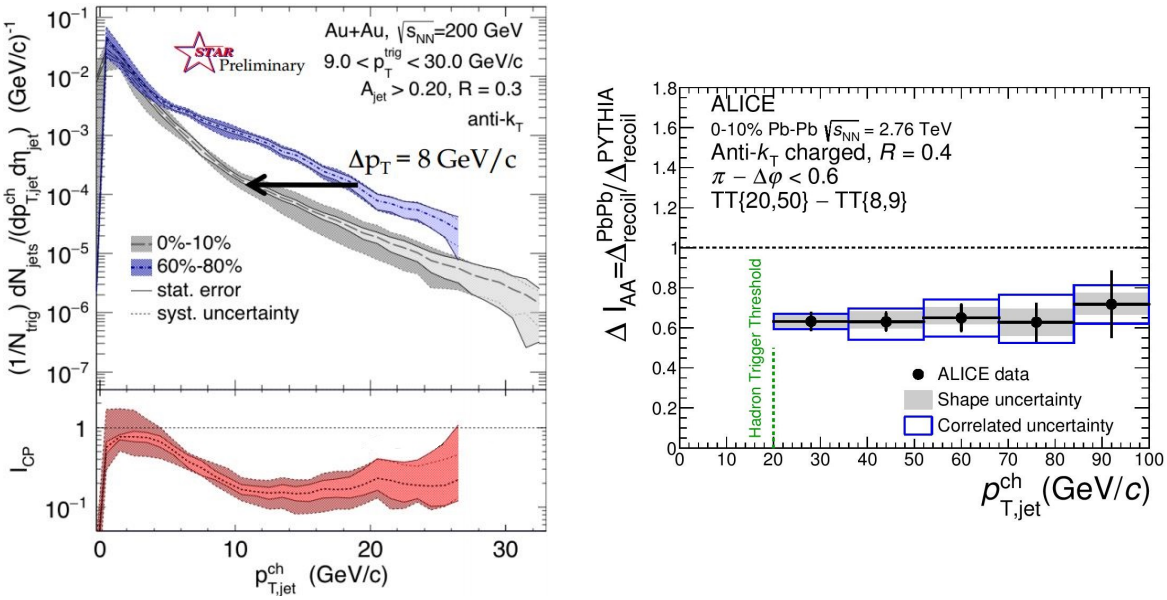

Figure 3.10: Left: Charged recoil jet spectrum for central and peripheral collisions $R = 0.3$ together with the nuclear modification I_{CP} [38]. Right: ΔI_{AA}, the ratio of Δ_{recoil} in Pb+Pb and PYTHIA p+p collisions at $\sqrt{s} = 2.76$ TeV for $R = 0.4$ [39].

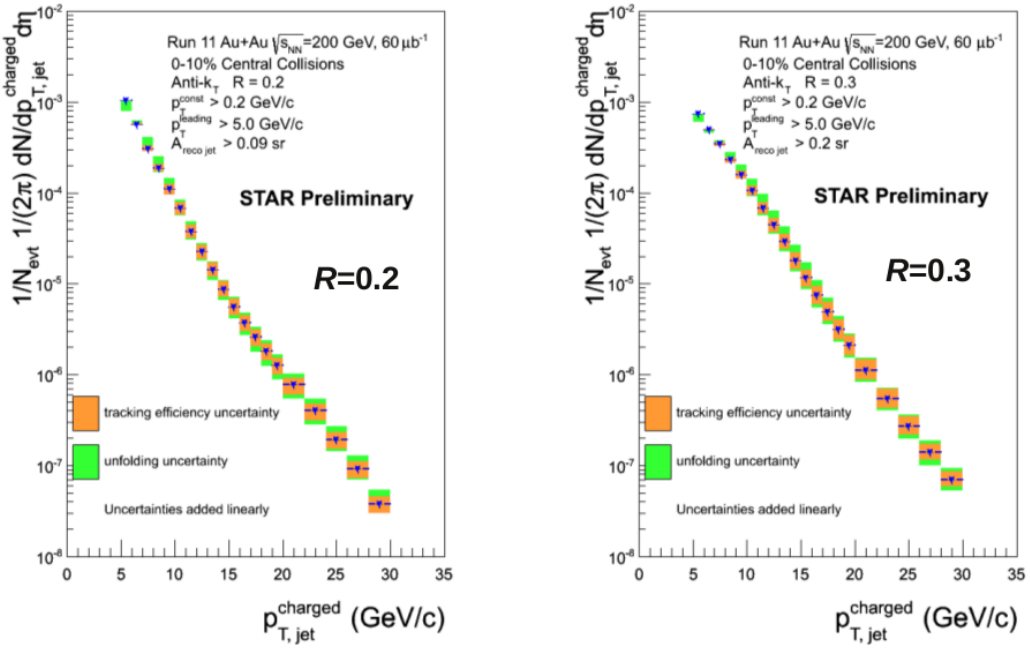

Figure 3.11: The corrected spectrum of inclusive charged jets in central Au+Au collisions at $\sqrt{s} = 200$ GeV for R=0.2 and 0.3 [40].

Chapter 4

Analysis of full jets

Full jet reconstruction provides a direct measurement of whole original energy of scattered partons before energy loss in the medium. We are not limited only to charged particles, but we accept also neutral component of the jet. This approach enables reconstruction of parton kinematics in unbiased way and also extends the kinematic reach of jet reconstruction in Au+Au collisions up to higher jet energies.

The main aim of this research project is the study of properties of fully reconstructed jets and its comparison to charged jets produced in Au+Au collisions at $\sqrt{s_{NN}}$= 200 GeV.

Charged tracks were measured by the Time Projection Chamber (TPC) and neutral energy by energy deposited in towers by Barrel ElectroMagnetic Calorimeter (BEMC) of the STAR detector. The analysis consists of following steps:

- Event selection.
- Track quality cuts.
- Study of data quality assurance, response of the BEMC and its time stability.
- Application of sequential recombination algorithm anti-k_T on data as a function of the centrality as well as the resolution parameter R to create uncorrected jet spectra.
- Background subtraction and the study of its influence on the jet spectra.
- Jet area cut study.
- Comparison of uncorrected full jet spectra with charged jet spectra with p_T cuts on leading hadron of the jet.

4.1 Data sample and event selection

Data used for this analysis are from Au+Au collisions at the center of mass energy of $\sqrt{s_{NN}} = 200$ GeV taken in the RHIC Run 11 by the STAR detector in year 2011. Au+Au collisions at $\sqrt{s_{NN}} = 200$ GeV were taken in approximately 7 weeks and 742 million events were collected. Then 66.6 million picoDST events were produced and I use 15.6 events with minimum bias (MB) trigger. PicoDST are smaller data files created from data measured by detector and contain only information interesting for our analysis e.g. information from the TPC, the BEMC and the VPD. Trigger IDs for minimum bias events are 350003, 350023, 350033 and 350043 (Label for these trigger IDs is "vpd-zdc-mb-protected"). Figure 4.1 shows distribution of the z-position of the primary vertex of all events. The primary vertex is a point where a collision happens. For the analysis we selected only events for which the longitudinal distance (z-axis direction) between the primary vertex and the center of the detector is less than 30 cm.

According to correspondence between centrality of a collision and reference multiplicity of charged particles derived from the Glauber model, events are sorted into several centrality classes. The relation between the value of charged-particle reference multiplicity and centrality of a collision can be found in Table 4.1 as well as in Figure 4.2, in which we can see also the relation between number of events and the value of reference multiplicity or centrality class.

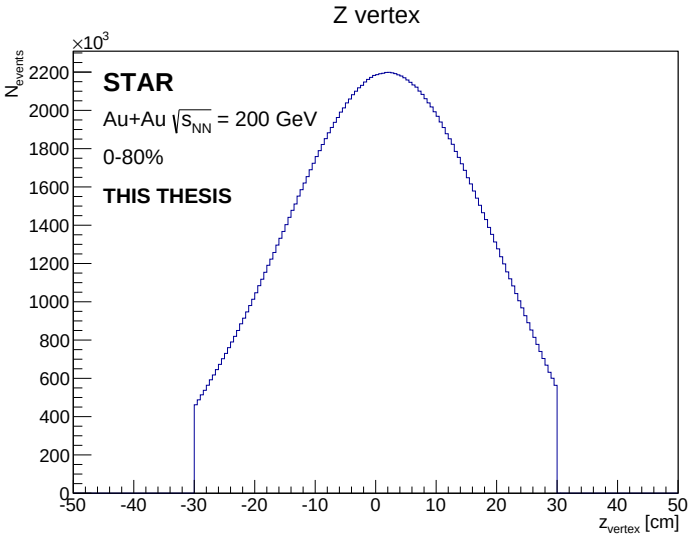

Figure 4.1: Distribution of the z-position of the primary vertex of all events with the cut $|V_z| < 30$ cm.

Centrality of collision	Centrality class	Reference multiplicity N_{ch}
most central	0-10 %	>396
central	10-20 %	281-396
semi central	20-40%	125-281
semi-peripheral	40-60%	43-125
peripheral	60-80%	10-43

Table 4.1: Centrality and centrality classes of Au+Au collisions at $\sqrt{s_{NN}} = 200$ GeV according to charged-particle reference multiplicity N_{ch}.

4.2 Charged track quality selection

This analysis uses charged tracks measured by the TPC of the STAR detector. Following track cuts are applied:

- distance of the closest approach of the track to primary vertex: DCA < 1.0 cm, depicted in Figure 4.3.
- number of track fit points = 14.
- ratio of number of track points in the TPC to maximum number of track points: 0.55.

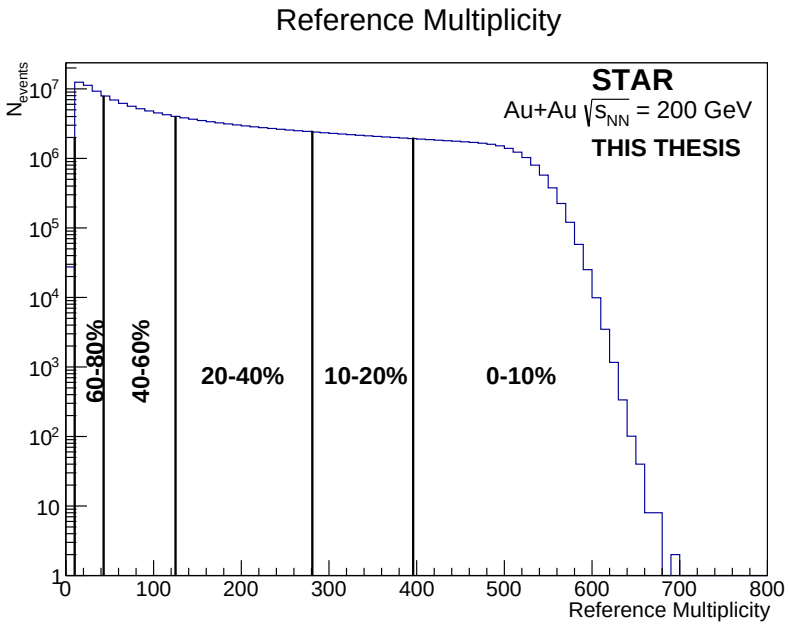

Figure 4.2: Reference charged-particle multiplicity of Au+Au collisions at $\sqrt{s_{NN}} = 200$ GeV with centrality classes cuts.

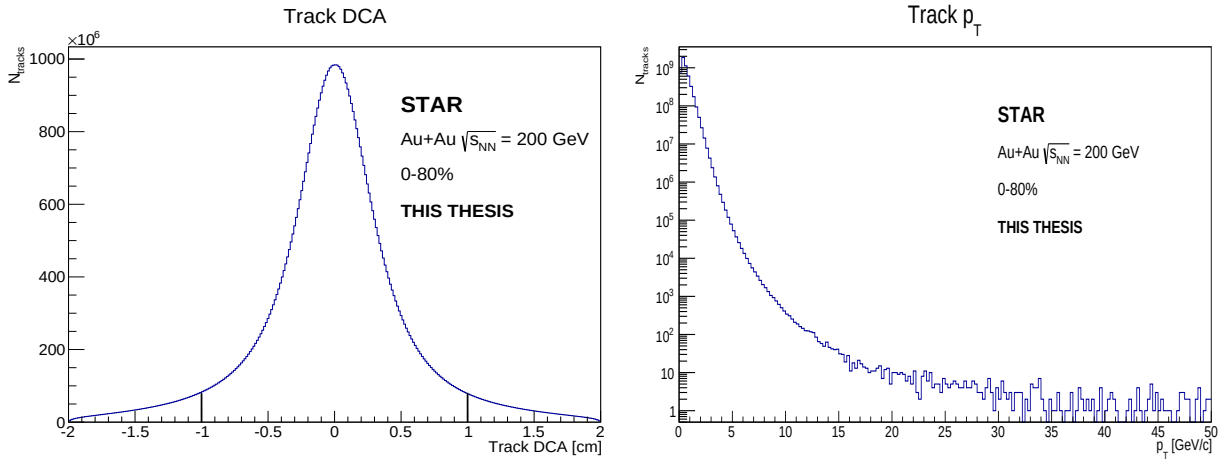

Figure 4.3: Charged track DCA cut (left) and track p_T distribution (right) in Au+Au collisions at $\sqrt{s_{NN}} = 200$ GeV.

Only tracks above $p_T = 200$ MeV/c are taken into jet reconstruction, because hadron tracking efficiency is low below this value. The right side of Figure 4.3 depicts track p_T distribution in all Au+Au events which fulfill the above mentioned selection criteria.

4.3 BEMC data quality assurance

The next step of the analysis is the study of data quality assurance of the BEMC, response of the BEMC and its time stability. First of all η - ϕ distribution of tower E_T was studied. Runs or events with many non-functional BEMC sectors were excluded as well. This problem was found in first two days of all 42 days of Au+Au collision data-taking. Figure 4.4 shows comparison of η - ϕ distribution of tower E_T in the first day of run with a sample of η - ϕ distribution of tower E_T in day which is included in the analysis. The sector around point $\eta = 0.3$ and $\phi = -0.8$ is non-functional during whole period of data-taking. The total number of towers in the BEMC is 4800, the effective size of each tower (BEMC resolution) is 0.05 x 0.05 = $\Delta\phi$ x $\Delta\eta$. In each run, approximately 2-3% of all towers are not functional. Some towers show higher energy deposited than the mean energy of all towers in a specific period of time. Such towers are referred to as hot towers and they have to be excluded from further analysis to avoid reconstruction of jets with abnormal high p_T. Towers in each run were ordered according to their mean energy deposit and towers with significantly higher energy deposit were removed as described below.

Figure 4.5 presents energy distribution in all towers and total energy deposit of all towers during Run 11 before and after exclusion of hot towers. We can see that the method described below successfully excluded towers with abnormal high energy deposit (bottom panel), removed strange peak at 30 GeV in the left top panel of Figure 4.5 and shifted E_T spectrum to lower energy values which is closer to reality.

The left panel of Figure 4.6 shows distribution of all towers according to their total deposited energy during Run 11. The distribution was fitted by Gaussian whose mean is $\mu = (7.25 \pm 0.01).10^6$ GeV and $\sigma = (6.93 \pm 0.1).10^5$ GeV. The cut for hot tower removal was determined to be about $8.9.10^6$ GeV, which corresponds to 2.5σ. From this point there are more towers with higher energy deposit than it would be expected. The right panel of Figure 4.6 expresses the number of physical run, in which an individual tower was considered to be a hot tower. In other words this figure represents time stability of hot towers in all runs. Total number of physical runs is 914. In each run, the mean energy deposit was determined and towers with energy deposit above approximately 2.5σ were labeled as hot. All towers which were labeled as hot towers at least in one physical run are shown in the right panel of Figure 4.6. Considering the fact that the majority of towers in Figure 4.6 remains hot during whole Run 11 and some another are hot at least one half of Run 11, we can neglect and exclude also the rest of towers which was labeled as hot towers only in few physical runs in order to simplify the code of the analysis. There is only one list containing 140 hot towers removed from whole Run 11 period.

In full jet analysis it is required to remove the energy deposited in BEMC by charged particles. Hadronic correction avoids double counting of charged particles that leave a track in the TPC and deposit energy in the BEMC. But energy deposition of charged particles in BEMC can be determined only statistically, because we do not know precisely the fraction of deposited charged-particle energy. The hadronic correction parameter of tower energy deposit was set to value 1.0, which means that whole fraction of charged track p_T is subtracted from deposited tower energy. But in the future more detailed study of looking for right hadronic correction parameter will be performed.

4.4 Jet reconstruction

Jets were reconstructed as a function of jet resolution parameter $R = 0.2, 0.3, 0.4$ as well as function of centrality in 5 centrality bins: 0-10%, 10-20%, 20-40%, 40-60%, 60-80%. There is a minimum p_T cut $p_T^{min} = 200$ MeV/c and maximum p_T cut $p_T^{max} = 30$ GeV/c on each jet constituent (each track or tower). Pseudorapidity interval cut $|\eta| < 1 - R$ based on the jet centroid was applied on each jet. This cut is also referred to as a fiducial cut which excludes particles of reconstructed jets out of range of the TPC and the BEMC acceptance. In the $\eta - \phi$ space there is almost an empty sector in the TPC and the BEMC which overlap with each other and therefore the number of jets there is low. The empty sector is depicted in the right panel of Figure 4.7 and it is located in the range of $\eta = 0 - 0.6$ and $\phi = 5 - 6$ and corresponds with the low energy area in $\eta - \phi$ distribution of track p_T in the left panel and with non-functional sector of the BEMC located around point: $\eta = 0.3$ and $\phi = -0.8$ in the left panel of Figure 4.4. It was considered

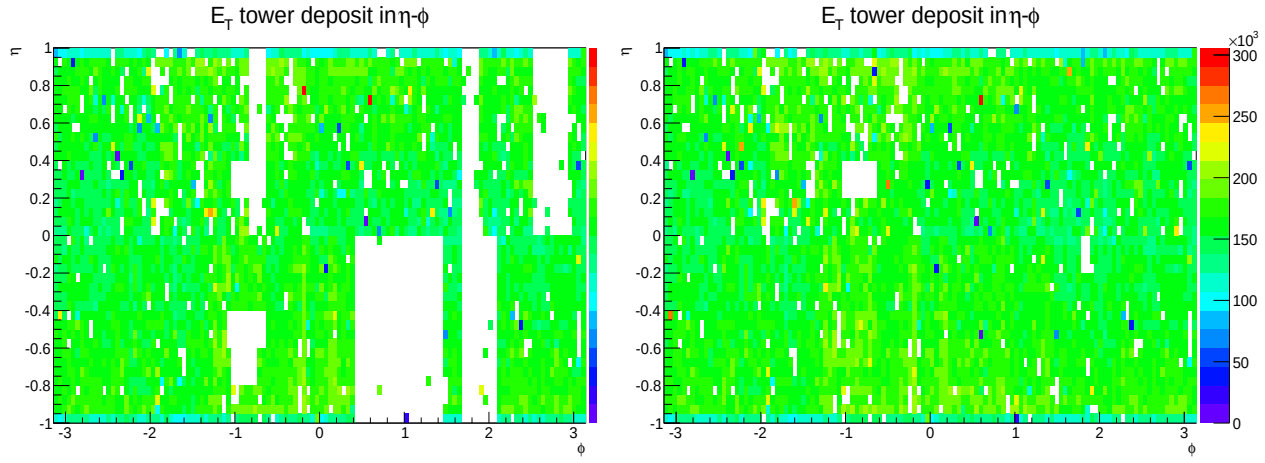

Figure 4.4: $\eta - \phi$ distribution of total tower E_T during first days of Run 11 (left) which are excluded from the analysis and a sample of $\eta - \phi$ distribution of total tower E_T (right) during day which is included in the analysis.

to exclude jets reconstructed in this sector, but no difference in jet spectra was observed and this sector is included in the analysis.

4.4.1 Background subtraction

The transverse momentum density of background ρ is estimated by using reconstruction of jets by k_T-algorithm. In each event, two highest p_T jets reconstructed by k_T algorithm were excluded from estimation of background energy density ρ, which was computed according to the following formula:

$$\rho = \text{median}\left(\frac{p_{T,i}}{A_i}\right), \tag{4.1}$$

where i runs over all reconstructed jets with transverse momentum $p_{T,i}$ and area of jet A_i in the event. Figures 4.8 present background energy density ρ dependence on the multiplicity of a collision for full jets, charged jets, full jets without hadronic correction, jets reconstructed only from BEMC data. This can be compared with the result from the ALICE experiment, which can be found in Figure 4.9.

The estimated background energy of full jets in central collisions is approximately $\rho = 62$ GeV/c with $\sigma = 8 - 9$ GeV/c. Charged jet background energy density is about $\rho = 30$ GeV/c with $\sigma = 3$ GeV/c. Figure 4.10 presents ρ estimation for each centrality class and resolution parameter R. Values of background energy for different resolution parameters almost overlap. For higher resolution parameter, the background energy is slightly higher. The value of background energy density in the central collision at ALICE is $\rho = 138.32 \pm 0.02$ GeV/c and $\sigma = 18.51 \pm 0.01$ GeV/c and for peripheral collisions 50-60% is $\rho = 12.05 \pm 0.01$ GeV/c and $\sigma = 3.41 \pm 0.01$ GeV/c[41]. Minimum jet constituent cut was $p_T = 150$ MeV/c. All values of the mean background energy density ρ with σ for all resolution parameters and centrality bins are summarized in Table 4.2 and compared with result from the ALICE experiment.

After background energy estimation, an event-by-event correction is provided for each jet p_T from which the median of jet energy density multiplied by the jet area A is subtracted:

$$p_{T,corr} = p_{T,uncorr} - A\rho, \tag{4.2}$$

where $p_{T,corr}$ is the momentum of a jet corrected on background effects unlike $p_{T,uncorr}$, which is measured and uncorrected jet momentum.

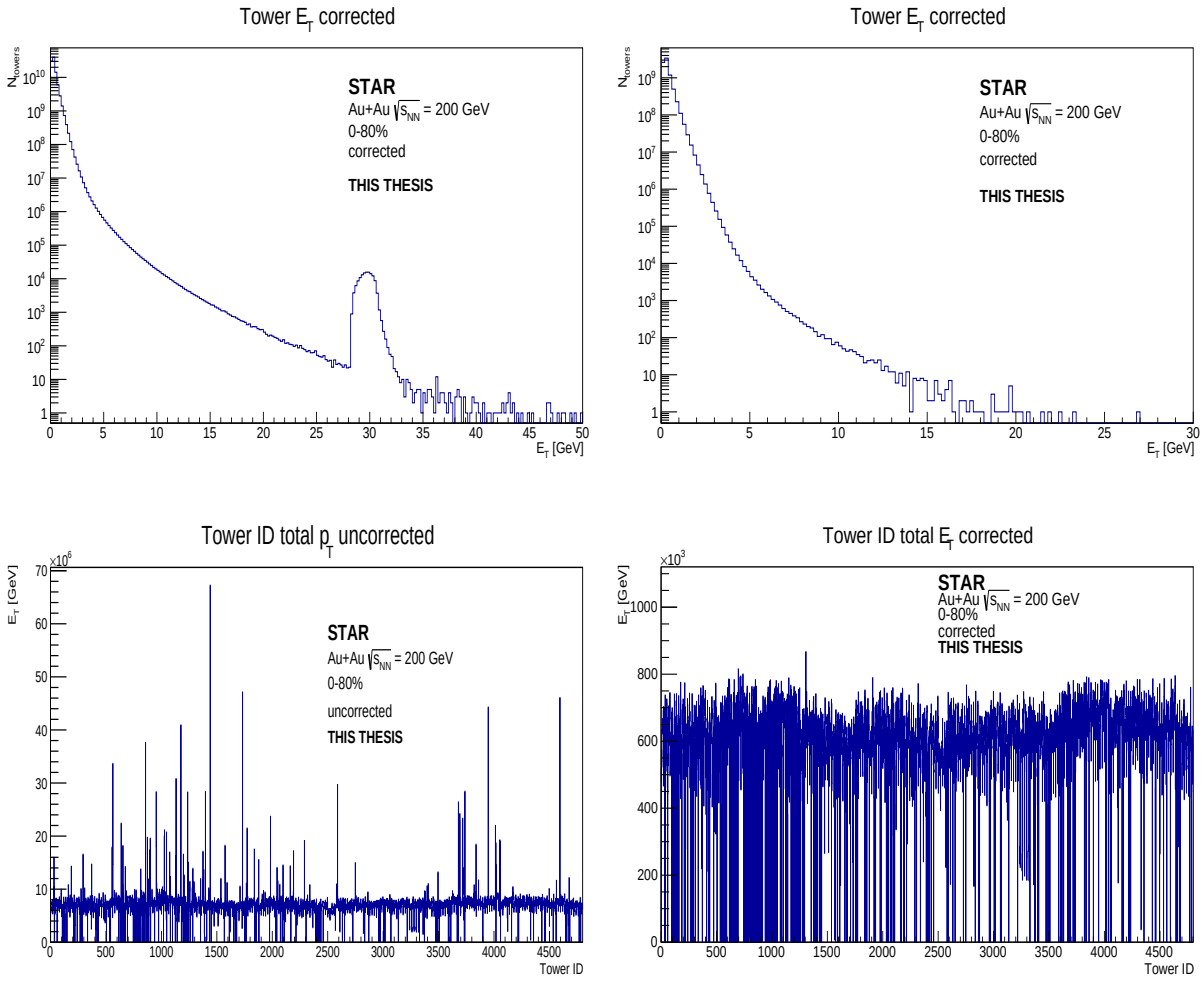

Figure 4.5: Tower p_T distribution (top) and total energy deposit in each tower (bottom) in Au+Au collisions at $\sqrt{s_{NN}} = 200$ GeV during Run 11 before (left) and after (right) exclusion of hot towers.

4.4.2 Jet area study

Figure 4.11 shows the jet area distribution versus jet p_T for full and charged jets with resolution parameter $R = 0.2$, 0.3, 0.4 in central collisions. There is a line which represents area cut on jets, only jet with area above this threshold are further accepted in the analysis. These cuts are listed in Table 4.3. Jet area cut is required to suppress jets reconstructed especially from the combinatorial background. Jets reconstructed with very low jet area do not have to be true jets, because they might comprise only from one high p_T particle. Jet area cut preserves true hard jets with high efficiency. Figure 4.12 presents jet area distribution of all reconstructed full and charged jets with the resolution parameter $R = 0.2$, 0.3, 0.4 in central collisions. This figure is a projection of the previous figure in centrality bin 0-10%. The significant number of low p_T jets with small area were excluded. Figure 4.13 depicts jet area distribution of all reconstructed full and charged jets with jet $p_T > 10$ GeV/c and the resolution parameter R= 0.2, 0.3, 0.4 in central collisions without any cut on the jet area. We can see that all jet area cuts are well defined and we obtain mainly hard jets.

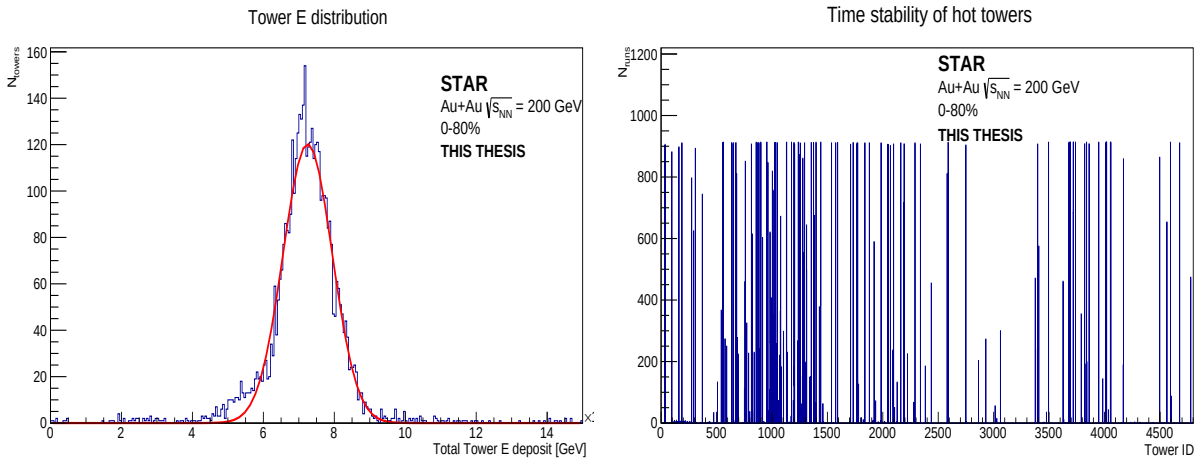

Figure 4.6: Tower ID distribution according to total deposited energy during Run 11 (left). The right part of figure expresses the rate of each tower in the number of physical runs, when the tower was considered to be a hot tower.

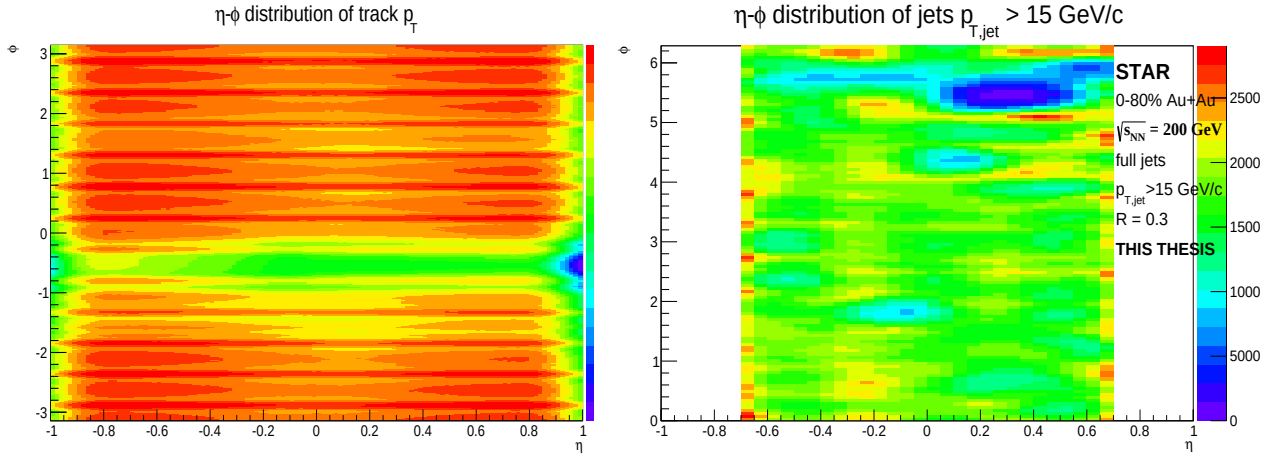

Figure 4.7: $\eta - \phi$ distribution of total track p_T during whole Run 11 (left) and $\eta - \phi$ distribution of reconstructed full jets (right) with $p_T > 15$ GeV and the resolution parameter $R = 0.3$ in Au+Au collisions at $\sqrt{s_{NN}} = 200$ GeV during whole Run 11.

4.4.3 Uncorrected inclusive full jet spectra

This section presents results from reconstruction of full jet spectra which are compared to charged jet spectra. These jets are not yet corrected for detector effects and background fluctuations. Jets were reconstructed as a function of jet resolution parameter $R = 0.2$, 0.3, 0.4 as well as function of centrality in 5 centrality bins: 0-10%, 10-20%, 20-40%, 40-60%, 60-80%.

Figure 4.14 presents full and charged jet spectrum corrected only for the average background energy density $< \rho >$ for three jet resolution parameters $R = 0.2$, 0.3, 0.4 reconstructed in Au+Au central and peripheral collisions at $\sqrt{s_{NN}} = 200$ GeV. We can see comparison of jet reconstructed with several resolution parameters and their different p_T range. As we can expect, the largest kinematic range has jet spectrum in central collisions with $R = 0.4$, because such jet collects more particles, thus the momentum

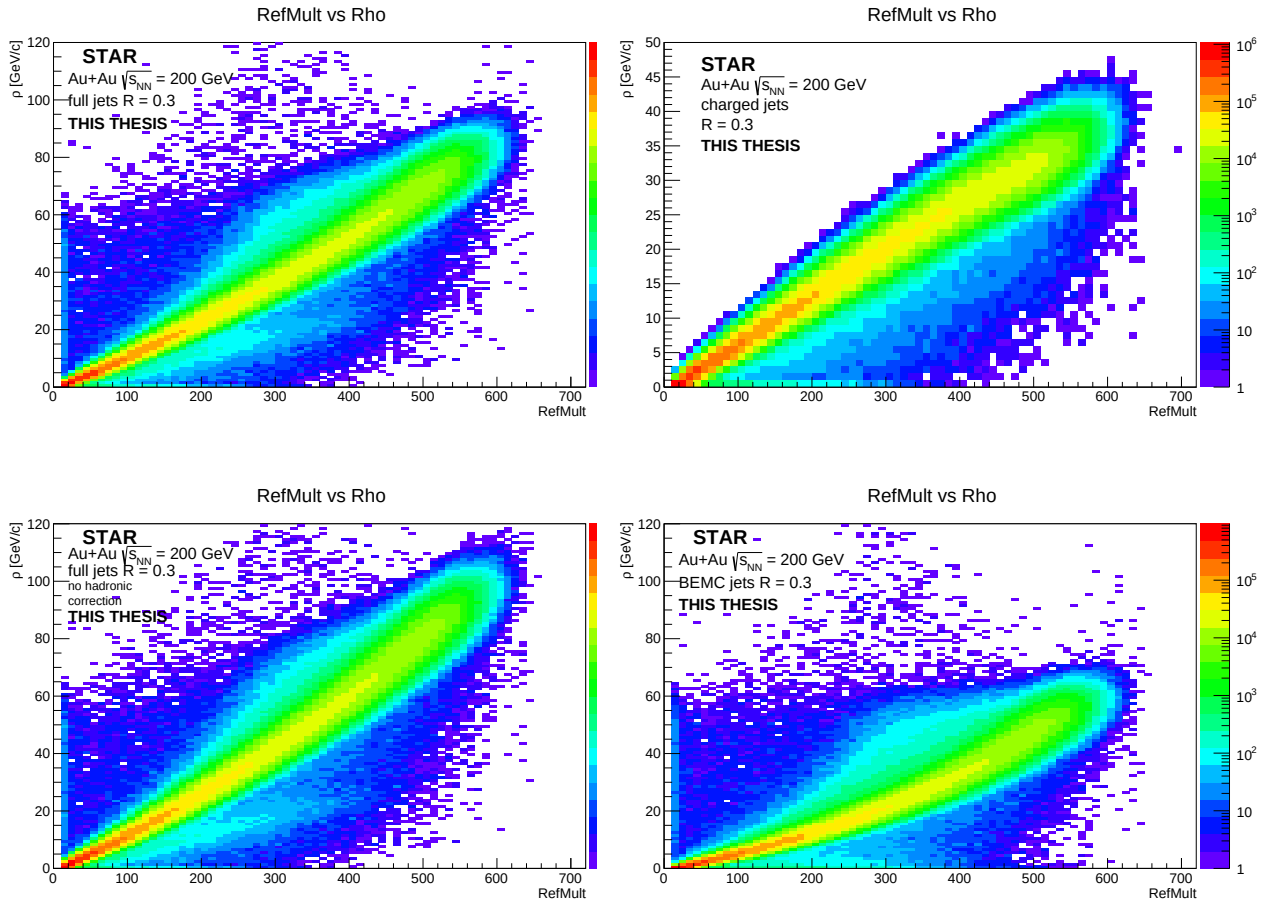

Figure 4.8: Background energy density ρ estimated from the median of full (top left) jets, charged jets (top right), full jets without hadronic correction (bottom left) and jets obtained only from BEMC data reconstructed by the k_T-algorithm with the resolution parameter $R = 0.3$ versus reference multiplicity of charged particles in Au+Au collisions at $\sqrt{s_{NN}} = 200$ GeV.

of the jet will be larger and the maximum p_T of this jet spectra is up to 50 GeV/c, while in charged jet spectrum, the maximum kinematic range reaches only 30-40 GeV/c. Central collisions show noticeable difference between resolution parameters but in comparison with peripheral collisions, difference is not so significant. Figures 4.15 and 4.16 show jet spectrum with three cuts applied on the momentum of the leading particle in a jet: $p_T > 0$, 2, 4, 6 GeV/c with resolution parameter $R = 0.3$ in all mentioned centrality bins. Cuts on the momentum of the leading hadron lead to suppression of combinatorial background and we can obtain only true high p_T jets. But on the other hand jet spectrum is more biased with smaller statistic. Figure 4.17 shows dependence of jet spectrum on centrality of a collision. Full and charged jets are reconstructed with the resolution parameter $R = 0.3$. By decreasing of centrality of the collision (from central to peripheral) we can observe narrowing of jet spectrum. It means that in central collisions there is more hard jets than in peripheral. Jet momentum is decreasing in the direction from central to peripheral collisions.

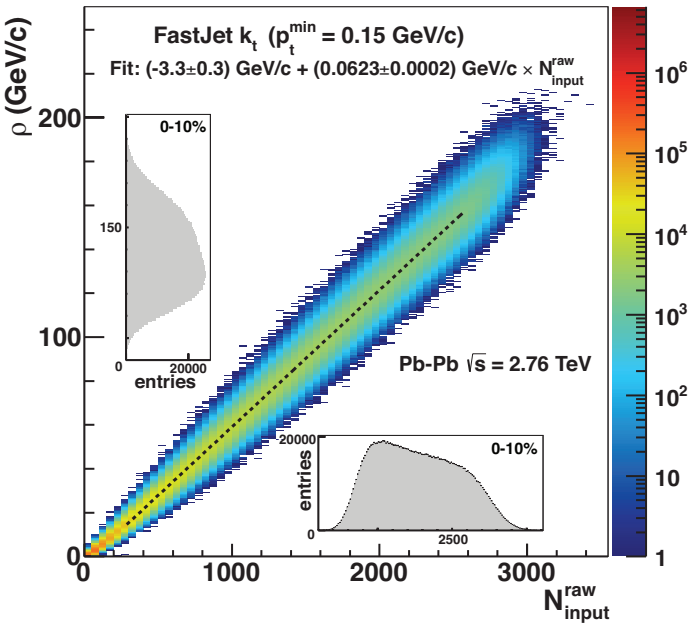

Figure 4.9: Background energy density ρ estimated from the median of charged jets reconstructed by the k_T-algorithm versus reference multiplicity of charged particles at the ALICE experiment in Pb+Pb collisions at $\sqrt{s_{NN}} = 2.76$ TeV .[41]

Centrality	R	ρ [GeV/c]	σ [GeV/c]
full jets			
0-10%	0.2	63.8	9.0
	0.3	63.1	8.9
	0.4	61.8	8.1
10-20%	0.2	42.4	6.5
	0.3	42.0	6.4
	0.4	41.1	6.4
20-40%	0.2	22.6	6.6
	0.3	22.5	6.5
	0.4	22.1	6.4
40-60%	0.2	7.8	3.2
	0.3	8.0	3.1
	0.4	7.9	3.1
60-80%	0.2	0.8	1.5
	0.3	1.8	1.6
	0.4	2.0	1.4
charged jets			
0-10%	0.2	30.3	3.3
	0.3	30.2	3.4
	0.4	29.6	3.5
charged jets ALICE			
0-10%	0.4	138.3	18.5
50-60%	0.4	12.1	3.3

Table 4.2: The mean background energy density ρ with σ and the resolution parameter R in all centrality classes of Au+Au collisions at $\sqrt{s_{NN}} = 200$ GeV for full jets and in central Au+Au collisions for charged jets. Results from STAR are compared to the mean background energy density ρ with σ and the resolution parameter $R = 0.4$ measured by the ALICE experiment in central 0-10% and peripheral 50-60% Pb+Pb collisions at $\sqrt{s_{NN}} = 2.76$ TeV.

R = 0.2	A > 0.09
R = 0.3	A > 0.2
R = 0.4	A > 0.4

Table 4.3: Jet area cut for each jet resolution parameter.

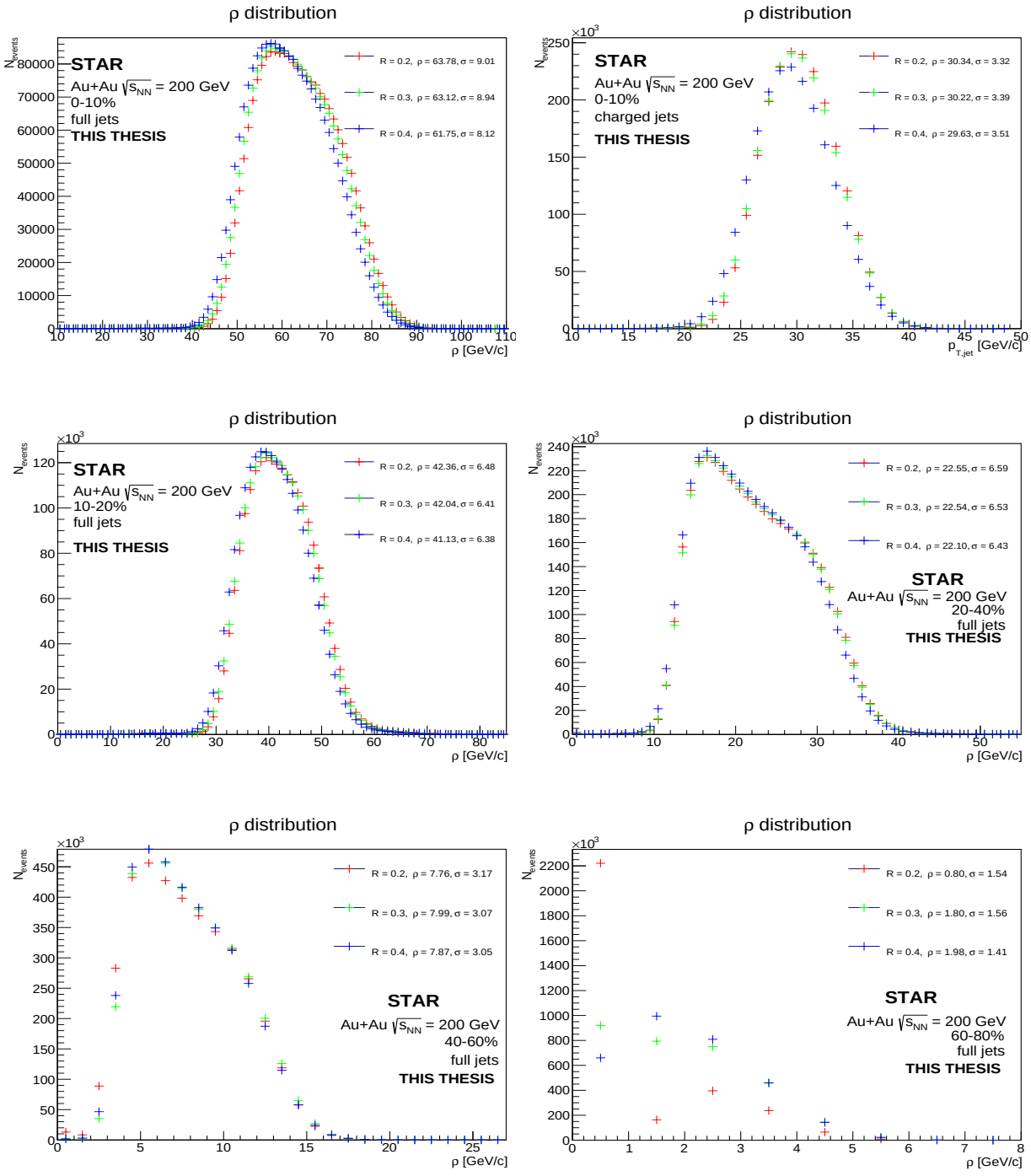

Figure 4.10: Background energy density for full jets in all centrality classes of Au+Au collisions at $\sqrt{s_{NN}} = 200$ GeV: 0-10% (top left), 10-20% (middle left), 20-40% (middle right), 40-60% (bottom left), 60-80% (bottom right) and for charged jets in central Au+Au collisions 0-10% (top right). The jet resolution parameter is $R = 0.2$, 0.3, 0.4 and the mean background energy density with σ are listed (see legend).

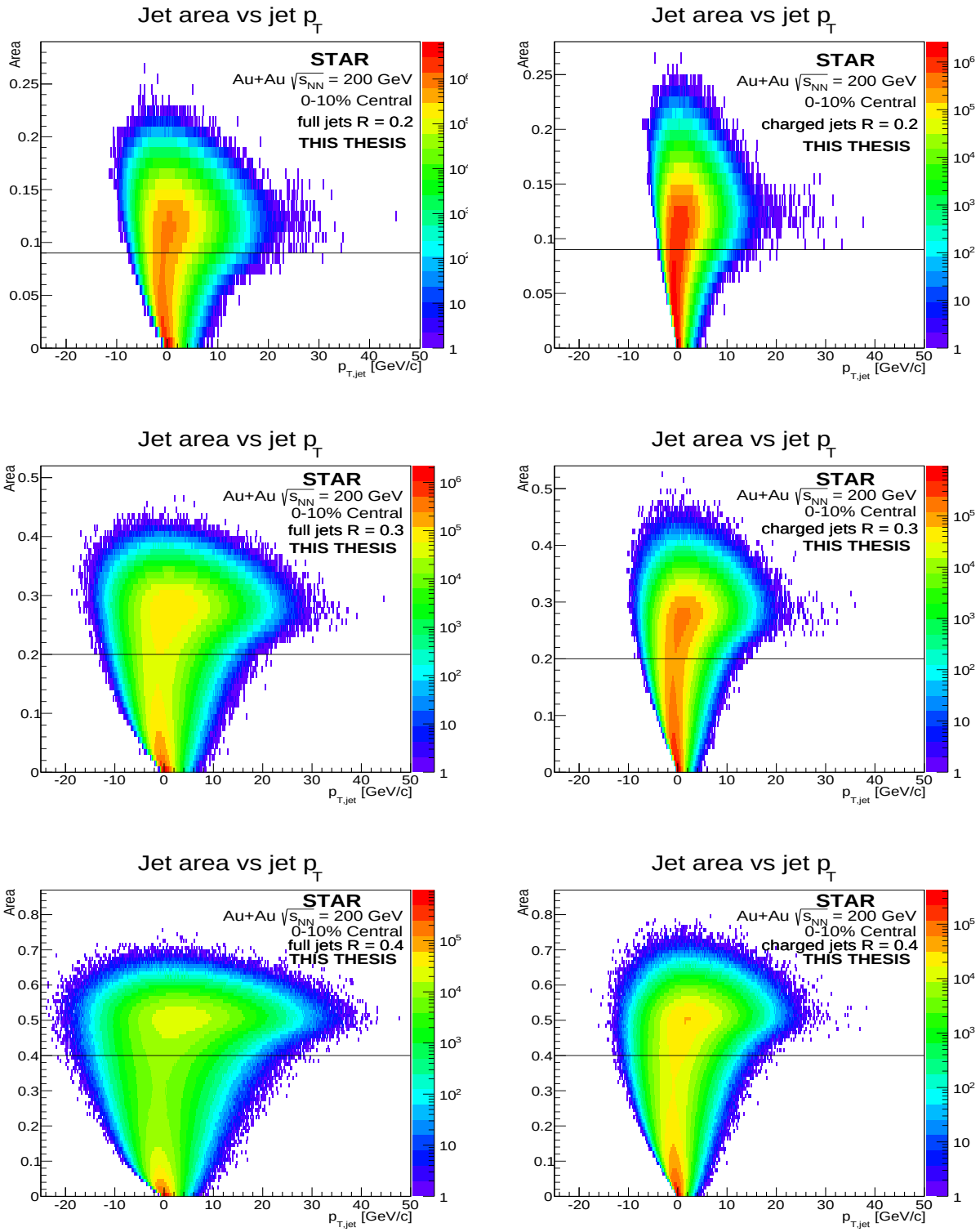

Figure 4.11: Jet area versus jet p_T for full (left) and charged (right) jets with the resolution parameter $R = 0.2$ (top),0.3 (middle), 0.4 (bottom) in central 0-10% Au+Au collisions at $\sqrt{s_{NN}} = 200$ GeV. The line represents cut on jet area.

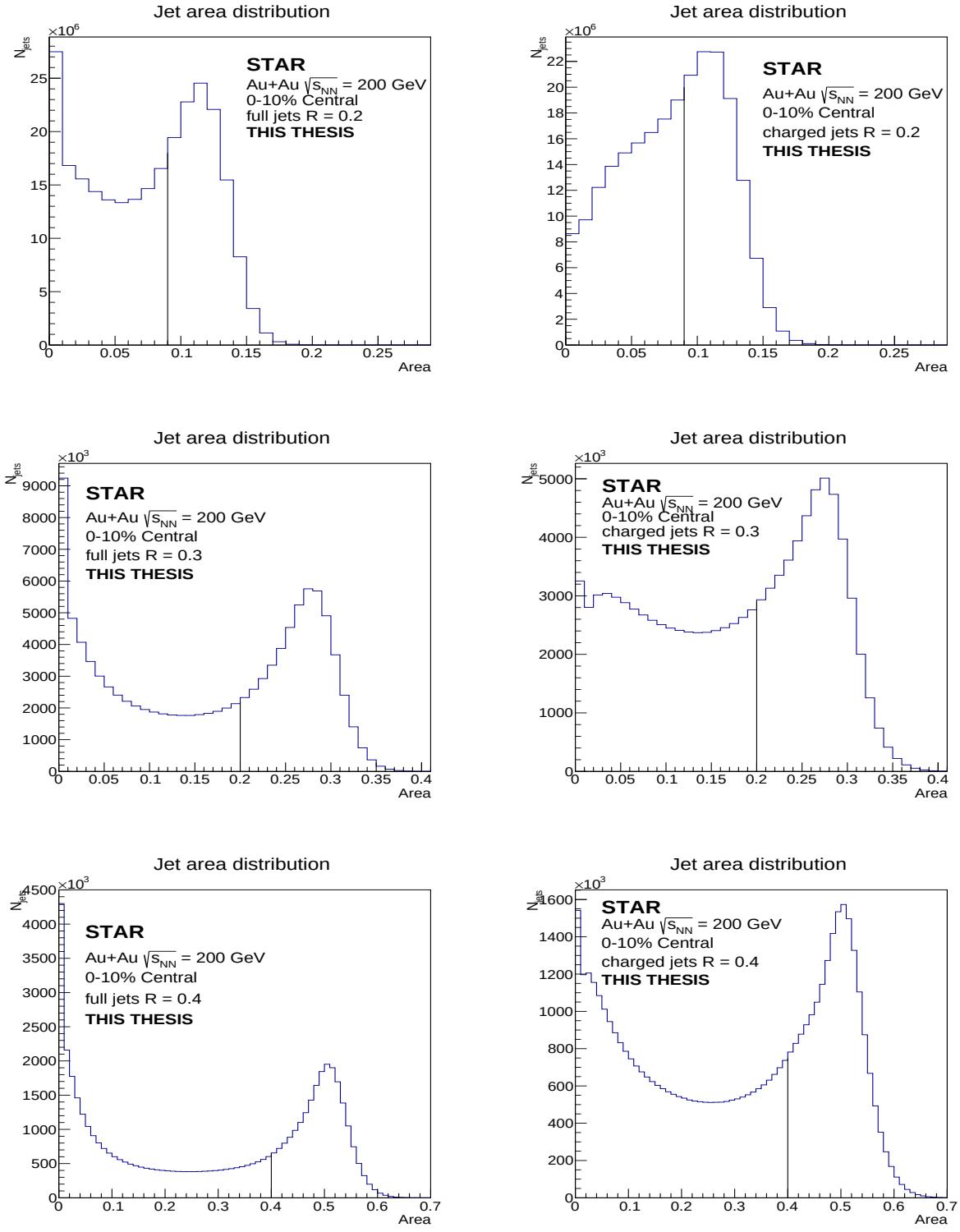

Figure 4.12: Jet area distribution for full (left) and charged (right) jets with the resolution parameter $R = 0.2$ (top),0.3 (middle), 0.4 (bottom) in central 0-10% Au+Au collisions at $\sqrt{s_{NN}} = 200$ GeV. The line represents cut on jet area.

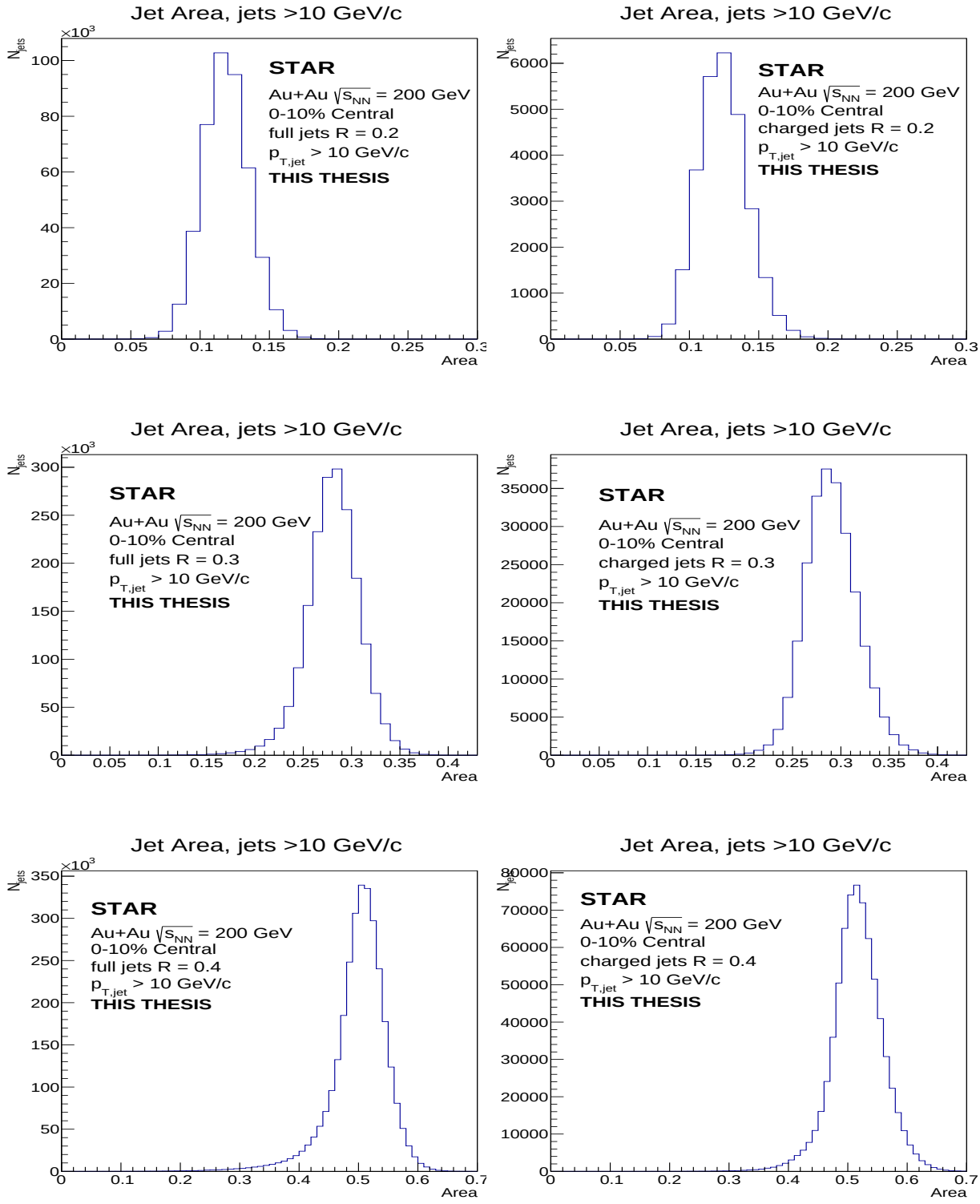

Figure 4.13: Area of full and charged jets > 10 GeV reconstructed with the resolution parameter $R = 0.2$ (top),0.3 (middle), 0.4 (bottom) in central 0-10% Au+Au collisions at $\sqrt{s_{NN}} = 200$ GeV.

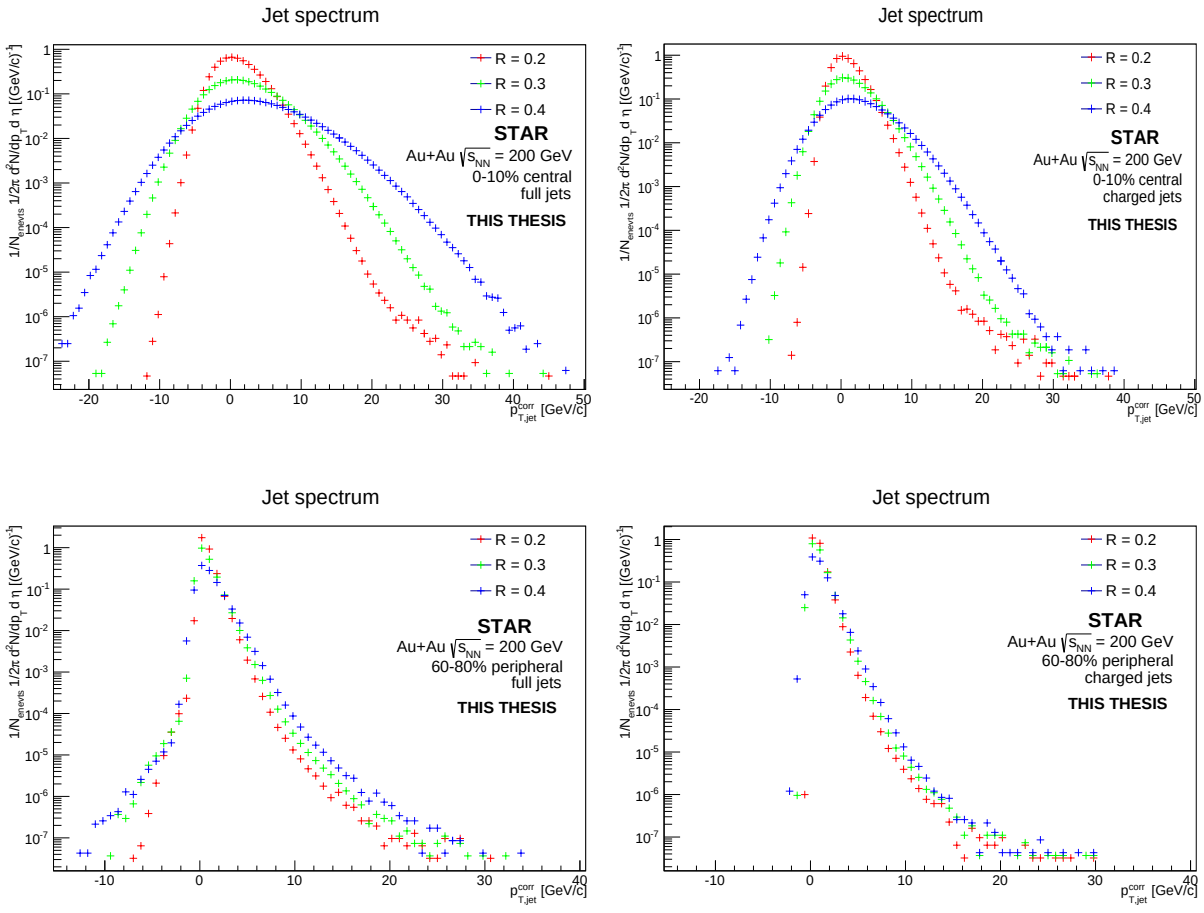

Figure 4.14: An uncorrected full (left) and charged (right) reconstructed jet spectrum in central 0-10% (top) and peripheral 60-80% (bottom) Au+Au collisions at $\sqrt{s_{NN}} = 200$ GeV with three resolution parameters: $R = 0.2, 0.3, 0.4$.

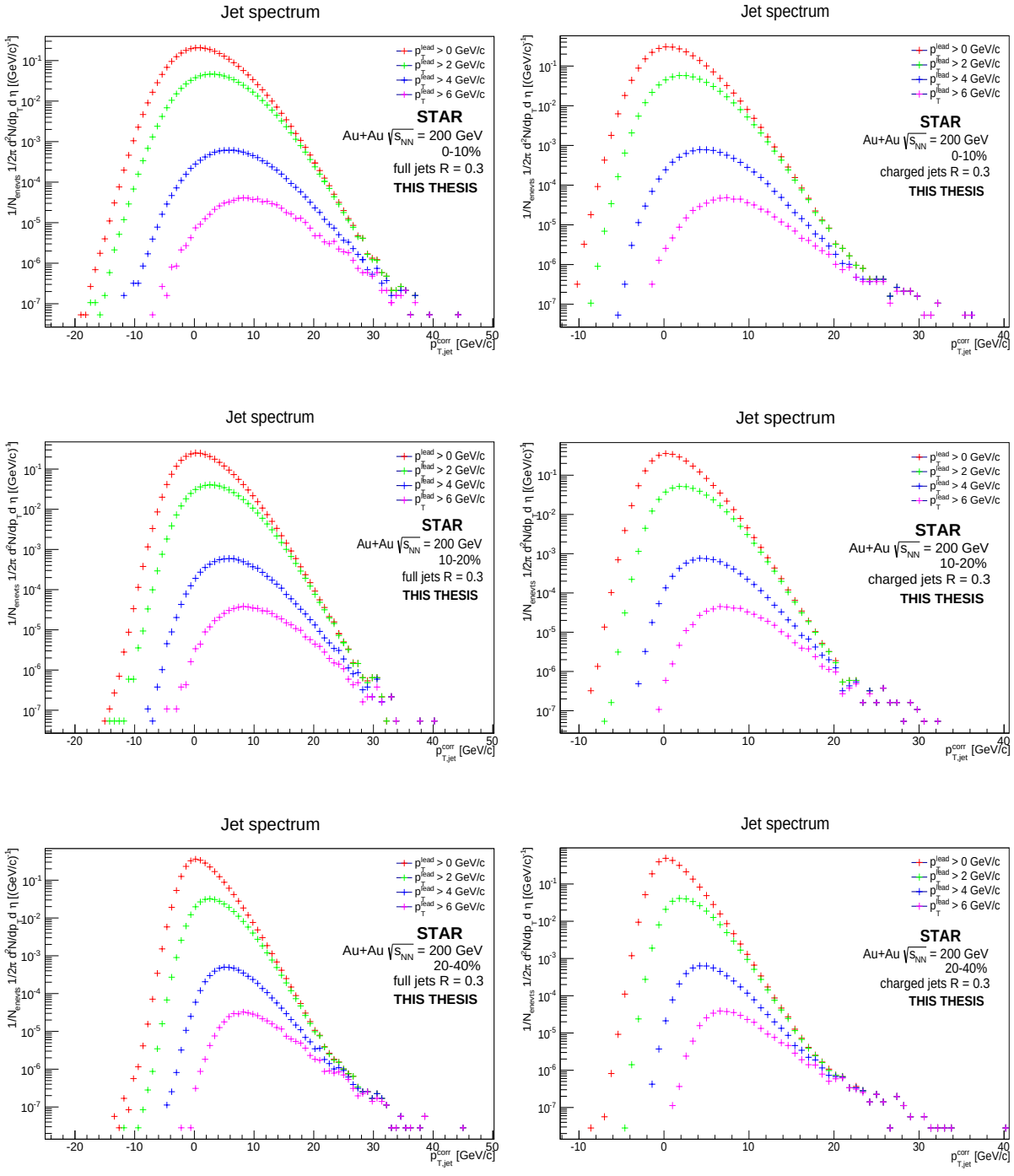

Figure 4.15: An uncorrected full (left) and charged (right) reconstructed jet spectrum of Au+Au collisions at $\sqrt{s_{NN}} = 200$ GeV in centrality 0-10% (top), 10-20% (middle) and 20-40% (bottom). The resolution parameter $R = 0.3$ and p_T leading cuts > 0, 2, 4, 6 GeV/c were used in this jet reconstruction.

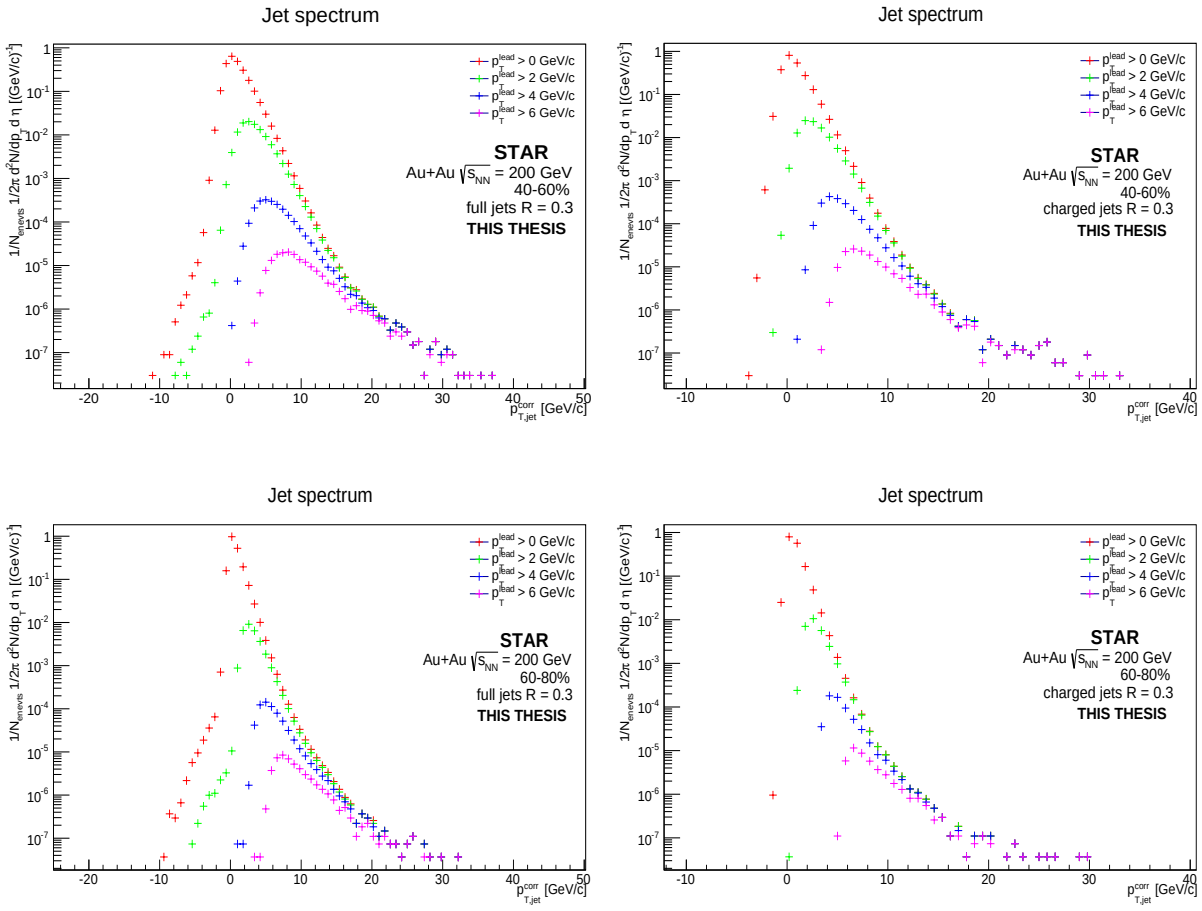

Figure 4.16: An uncorrected full (left) and charged (right) reconstructed jet spectrum of Au+Au collisions at $\sqrt{s_{NN}} = 200$ GeV in centrality 40-60% (top) and 60-80% (bottom). The resolution parameter $R = 0.3$ and p_T leading cuts > 0, 2, 4, 6 GeV/c were used in this jet reconstruction.

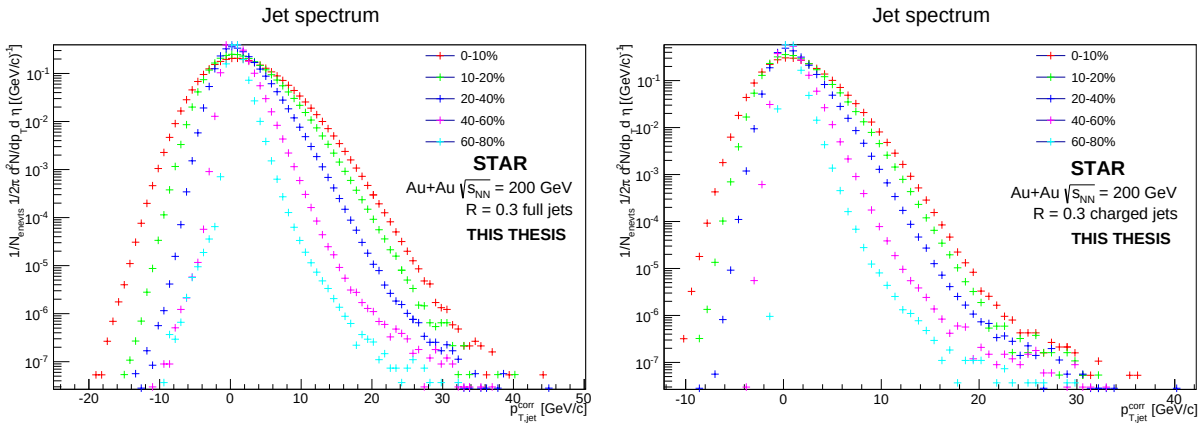

Figure 4.17: An uncorrected full (left) and charged (right) reconstructed jet spectrum of Au+Au collisions at $\sqrt{s_{NN}} = 200$ GeV with the resolution parameter $R = 0.3$ for all centrality classes (see legend).

Summary and Outlook

The main subject of this research project is to acquaint with jet physics and present the beginning of the jet analysis in Au+Au collisions at $\sqrt{s_{NN}} = 200$ GeV at the STAR experiment.

Experiments at RHIC and at the LHC are utilized for research of quark-gluon plasma which is a new state of hot and dense strongly interacting nuclear matter consisting of free partons. QGP is theoretically predicted by Quantum Chromodynamics and exists at extremely high temperature and density. QGP is supposed to be formed in ultra-relativistic heavy-ion collision which is a dynamical process with large energy transfer and lasts only few femtoseconds. During hard scattering, partons of incoming nuclei undergo fragmentation and hadronisation resulting in jets, one of the most important probe of QGP.

Jets are collimated sprays of particles that are produced immediately after the collision. Due to elastic and inelastic interactions of hard partons with QGP the energy of partons is reduced in comparison with p+p collisions. It means that jets might be quenched and modified by medium and this phenomenon is referred to as a jet quenching which helps in the research of QGP and the strong interaction. Jet-finding algorithms are used for jet reconstruction and their main goal is to cluster a set of charged tracks and neutral energy deposited in towers into jets. The algorithm selects a set of particles, which are typically emitted close to each other in an angle and combines their momenta to form the momentum of a jet. Jet resembles kinematic properties of the original parton. Therefore jet reconstruction allows to access early stages of the collision. Jet reconstruction is successful in p+p collisions, while in the heavy-ion collision environment is more complicated due to the large fluctuating background.

Full jet reconstruction provides a direct measurement of whole original energy of scattered partons before energy loss in the medium. We are not limited only to charged particles, but we accept also neutral component of the jet. This approach enables reconstruction of parton kinematics in unbiased way and also extends the kinematic reach of jet reconstruction in Au+Au collisions up to higher jet energies.

The main part of the research project presents results of full jet reconstruction in Au+Au collisions at $\sqrt{s_{NN}} = 200$ GeV collected in Run 11. Firstly, suitable events were selected and cuts on charged tracks were applied. Subsequently the study of data quality assurance, response of the BEMC and its time stability was performed. Hot towers which are towers with excessive energy deposit were excluded from the jet analysis to avoid jet reconstruction with abnormal high energy. Then the sequential recombination algorithm anti-k_T was applied on data as a function of the centrality as well as the resolution parameter R to create uncorrected jet spectra. This was followed by background subtraction, the study of its influence on jet spectra and the study of jet area cut. All results of uncorrected full jet spectra were compared with charged jet spectra with p_T cuts on the leading parton of the jet.

The analysis will continue by several subsequent steps which will lead to true jet spectra. The next step is computation of δp_T which is difference in transverse momentum between reconstructed and simulated jet embedded to real event: $\delta p_T = p_{T,jet}^{corr} - p_{T,jet}^{emb}$. This helps to obtain the response matrix, which gives the probability to measure true value of jet momentum. After that, unfolding of measured spectra will take place. These procedures represent correction of jet spectra on detector effects. It is also necessary to perform the study of the most correct value of the hadronic correction parameter, calculate efficiency and systematics errors. The analysis will result in computation of the nuclear modification factor R_{AA} of fully reconstructed jets. It is possible that full jet analysis will be performed also on data from Run 2014.

Bibliography

[1] K. Yagi et al., *Quark-gluon plasma*, Cambridge University Press, 2005.

[2] R. Stock, Relativistic Nucleus-Nucleus Collisions and the QCD Matter Phase Diagram, arXiv: 0807.1610v1 (2008).

[3] The Phases of QCD, http://www.bnl.gov/today/body_pics/2010/07/phases-of-qcd-350px.jpg [online 28.5.2015]

[4] Sarkar, Satz, Sinha, *The Physics of the Quark-Gluon Plasma*, Springer, 2009

[5] M. Kliemant, R. Sahoo, T. Schuster and R. Stock, Global Properties of Nucleus-Nucleus Collisions, Lect. Notes Phys. **785** (2010) 23 [arXiv:0809.2482 [nucl-ex]].

[6] M. L. Miller, K. Reygers, S. J. Sanders and P. Steinberg, Glauber modeling in high energy nuclear collisions, Ann. Rev. Nucl. Part. Sci. **57** (2007) 205 [nucl-ex/0701025].

[7] C. Nonaka and M. Asakawa, Modeling a Realistic Dynamical Model for High Energy Heavy Ion Collisions, PTEP **2012** (2012) 01A208 [arXiv:1204.4795 [nucl-th]].

[8] J. Adam *et al.* [ALICE Collaboration], Measurement of charged jet production cross sections and nuclear modification in p-Pb collisions at $\sqrt{s_{NN}} = 5.02$ TeV, arXiv:1503.00681.

[9] M. Shao [STAR Collaboration], Cronin effect at RHIC, AIP Conf. Proc. **828** (2006) 49.

[10] J. Adams *et al.* [STAR Collaboration], Evidence from d + Au measurements for final state suppression of high p(T) hadrons in Au+Au collisions at RHIC, Phys. Rev. Lett. **91** (2003) 072304 [nucl-ex/0306024].

[11] D. Barton *et al.* [BNL], Electron Beam Ion Source Pre-Injector Project, Conceptual Design Report, https://www.bnl.gov/cad/accelerator/docs/pdf/EBISDesignReportl.pdf [online 24.5.2016]

[12] G. Odyniec, The RHIC Beam Energy Scan program in STAR and what's next ..., J. Phys. Conf. Ser. **455** (2013) 012037.

[13] K. Kajimoto, A Large Area Time of Flight Detector for the STAR Experiment at RHIC, Ph.D thesis; U. of Texas at Austin (2009).

[14] M. J. Tannenbaum, Highlights from BNL-RHIC, Subnucl. Ser. **50** (2014) 347 [arXiv:1302.1833 [nucl-ex]].

[15] K. H. Ackermann *et al.* [STAR Collaboration], STAR detector overview, Nucl. Instrum. Meth. A **499** (2003) 624.

[16] O. Rusňáková, Measurements of non-photonic electrons in STAR, Hot Quarks 2014 presentation, 2014

[17] M. Anderson, J. Berkovitz, W. Betts et.al, The STAR Time Projection Chamber: A Unique Tool for Studying High Multiplicity Events at RHIC, 2003 arXiv:nucl-ex/0301015v1

[18] M. Shao, O. Y. Barannikova, X. Dong, Y. Fisyak, L. Ruan, P. Sorensen and Z. Xu, Extensive particle identification with TPC and TOF at the STAR experiment, Nucl. Instrum. Meth. A **558** (2006) 419 [nucl-ex/0505026].

[19] M. Beddo *et al.* [STAR Collaboration], The STAR barrel electromagnetic calorimeter, Nucl. Instrum. Meth. A **499** (2003) 725.

[20] C. Yang *et al.*, Calibration and performance of the STAR Muon Telescope Detector using cosmic rays, Nucl. Instrum. Meth. A **762** (2014) 1 [arXiv:1402.1078 [physics.ins-det]].

[21] A Brief Introduction to the STAR Heavy Flavor Tracker http://rnc.lbl.gov/ jhthomas/public/HeavyFlavorTracker/ [online 12.6.2015]

[22] F.S. Bieser et al, The STAR Trigger, https://www.star.bnl.gov/public/tpc/ NimPapers/trigger/trigger_nim.pdf [online 13.6.2015]

[23] X. N. Wang, Why the observed jet quenching at RHIC is due to parton energy loss, Phys. Lett. B **579** (2004) 299 [nucl-th/0307036]. alebo

[24] G. Aad et al. (ATLAS Collaboration), Observation of a Centrality Dependent Dijet Asymmetry in Lead-Lead Collisions at $\sqrt{s_{NN}} = 2.76$ TeV with the ATLAS Detector at the LHC Phys. Rev. Lett. 105

[25] D. d'Enterria, Jet quenching, arXiv:0902.2011v2, 2009

[26] Jet quenching, http://www.ellipsix.net/uploads/_9tb/atlas-jetquenching.png [online 28.5.2015]

[27] Matteo Cacciari and Gavin P. Salam. Jet clustering in particle physics, via a dynamic nearest neighbour graph implemented with CGAL. 2006 http://www.lpthe.jussieu.fr/ salam/repository/docs/kt-cgta-v2.pdf [online 8.6.2015]

[28] G. C. Blazey et al., Run II jet physics, hep-ex/0005012

[29] H. Caines [STAR Collaboration], Jet and Underlying Event Measurements in P+P Collisions at RHIC, Int. J. Mod. Phys. E **20** (2011) 1578 [arXiv:1011.4614 [nucl-ex]].

[30] G. P. Salam, Towards Jetography, Eur. Phys. J. C **67** (2010) 637 [arXiv:0906.1833 [hep-ph]].

[31] M. Cacciari and G. P. Salam, Dispelling the N^3 myth for the k_t jet-finder, Phys. Lett. B **641** (2006) 57 [hep-ph/0512210].

[32] G. P. Salam and G. Soyez, A Practical Seedless Infrared-Safe Cone jet algorithm, JHEP **0705** (2007) 086 [arXiv:0704.0292 [hep-ph]].

[33] M. Cacciari, G. P. Salam and G. Soyez, The Anti-k(t) jet clustering algorithm, JHEP **0804** (2008) 063 [arXiv:0802.1189 [hep-ph]].

[34] M. Cacciari, G. P. Salam and G. Soyez, The Catchment Area of Jets, JHEP **0804** (2008) 005 [arXiv:0802.1188 [hep-ph]].

[35] G. Soyez, Jet areas as a tool for background subtraction, arXiv:0905.2851 [hep-ph].

[36] M. Cacciari, G. P. Salam and G. Soyez, FastJet user manual, Eur. Phys. J. C **72** (2012) 1896 [arXiv:1111.6097 [hep-ph]].

[37] M. Ploskon [STAR Collaboration], Inclusive cross section and correlations of fully reconstructed jets in $\sqrt{s_{NN}}$ = 200 GEV Au+Au and p+p collisions, Nucl. Phys. A **830** (2009) 255C [arXiv:0908.1799 [nucl-ex]].

[38] P. M. Jacobs *et al.* [STAR Collaboration], Measurements of jet quenching with semi-inclusive charged jet distributions in $Au + Au$ collisions at $\sqrt{s_{NN}}$=200 GeV, arXiv:1512.08784 [nucl-ex].

[39] J. Adam *et al.* [ALICE Collaboration], Measurement of jet quenching with semi-inclusive hadron-jet distributions in central Pb-Pb collisions at $\sqrt{\mathbf{s_{NN}}}$ = 2.76 TeV, arXiv:1506.03984 [nucl-ex].

[40] J. Rusňák [STAR Collaboration], Charged jet reconstruction in Au+Au collisions at $\sqrt{s_{NN}}$ = 200 GeV at RHIC, arXiv:1412.2111 [hep-ex].

[41] B. Abelev *et al.* [ALICE Collaboration], Measurement of Event Background Fluctuations for Charged Particle Jet Reconstruction in Pb-Pb collisions at $\sqrt{s_{NN}}$ = 2.76 TeV, JHEP **1203** (2012) 053 [arXiv:1201.2423 [hep-ex]].